Anti- and Pro-tumor Functions of Distinct Regulatory T Cell Subsets in Colorectal Cancer

Xiao Huang[1,9], Dan Feng[2,9], Sneha Mitra[3,9], Emma S. Andretta[1], Nima B. Hooshdaran[1,4], Aazam P. Ghelani[5], Eric Y. Wang[1,6,7], Joe N. Frost[1], Victoria Lawless[1,6,7], Aparna Vancheswaran[1], Qingwen Jiang[8], Christina S. Leslie[3,10], Alexander Y. Rudensky[1,10]

1. Immunology Program, Sloan Kettering Institute, Memorial Sloan Kettering Cancer Center, New York, NY, USA
2. Tisch Cancer Institute, Icahn School of Medicine at Mount Sinai, New York, NY, USA
3. Computational and Systems Biology Program, Sloan Kettering Institute, Memorial Sloan Kettering Cancer Center, New York, NY, USA
4. Louis V. Gerstner Jr Graduate School of Biomedical Sciences, Memorial Sloan Kettering Cancer Center, New York, NY, USA
5. Immunology and Microbial Pathogenesis Program, Weill Cornell Graduate School of Medical Sciences, New York, NY, USA
6. Tri-Institutional MD-PhD Program, Weill Cornell Medicine, The Rockefeller University and Memorial Sloan Kettering Cancer Center, New York, NY, USA
7. Immunology and Microbial Pathogenesis Program, Weill Cornell Medicine Graduate School of Medical Sciences, New York, NY, USA
8. Molecular Pharmacology Program, Sloan Kettering Institute, Memorial Sloan Kettering Cancer Center, New York, NY, USA
9. These authors contributed equally to the manuscript.
10. Corresponding authors

Summary

Regulatory T (Treg) cells are considered major contributors to the growth of solid organ tumors, with the notable exception of colorectal cancer (CRC), despite the documented abundance of Treg cells in CRC. Here, we demonstrate that IL-10^{+} and IL-10^{-} Treg cells constitute two distinct subsets with opposing functions: IL-10^{+} Treg cells counteract, while IL-10^{-} Treg cells promote, the growth of genetically engineered CRC tumors. Our findings suggest that the tumor-suppressive function of IL-10^{+} Treg cells is mediated by their suppression of effector CD4^{+} T cell production of IL-17, a cytokine that directly stimulates CRC tumor cell proliferation. Consistently, IL-10^{+} Treg cells were more abundant in both mouse and human CRC tumors than in tumor-adjacent normal colon tissue, whereas IL-10^{-} Treg cells exhibited the opposite distribution. Furthermore, gene expression signatures associated with IL-10^{+} and IL-10^{-} Treg cells correlated with better and worse disease prognoses in human CRC, respectively. This functional dichotomy between Treg subsets provides a rationale for therapeutic strategies aimed at selectively targeting pro-tumoral Treg cells while preserving their anti-tumoral counterparts across various barrier tissue cancers that harbor both subsets.

INTRODUCTION

Regulatory T (Treg) cells, expressing the transcription factor *Foxp3*, carry out a wide range of functions essential for organismal physiology and fitness in health and disease. By modulating innate and adaptive immune responses, they prevent fatal autoimmunity and inflammation while preserving tissue function by limiting both microbe-induced inflammation, associated with host-commensal interactions or infections, and sterile metabolic-induced inflammation. Additionally, Treg cells directly promote tissue repair during injuries by producing factors that support tissue maintenance and differentiation and partaking in tissue stem cell niches[1]. Parallel to the effector arm of the adaptive immune system, Treg cells patrol the organism through recirculation and residence in the secondary lymphoid organs. In addition, they seed non-lymphoid tissues, particularly the barrier sites such as the gastrointestinal (GI) and genital tracts, skin, and airways. In these tissues, exposed to a variety of biotic and abiotic stressors, Treg cells establish and maintain immunological tolerance and limit inflammation through diverse immunosuppressive mechanisms[2,3].

Both the tolerogenic and tissue-maintenance functions of Treg cells feature prominently in solid organ cancers, where they assume a highly activated state. Tumoral Treg cells are thought to regulate activities of other accessory cells of immune and non-immune origin in the tumor microenvironment (TME) or act on tumors directly to favor tumor progression. The pronounced enrichment of tumor-associated Treg cells in solid organ cancers, generally linked to a poor prognosis[4-10], has inspired major recent efforts towards development of strategies for targeting of these cells as a novel means of immunotherapy. In support of these efforts, depletion of Treg cells in experimental solid organ cancer models including PD-1 and CTLA-4 blockade-resistant genetically induced tumors and orthotopically transplanted cell lines derived from these tumors resulted in their pronounced restraint or rejection[11-13]. In contrast to a broad consensus on tumor-supportive functions of Treg cells in the vast majority of the established tumors, colorectal cancer (CRC), which ranks as the as the second leading cause of cancer-related mortality

worldwide[14], appears to be an exception. In this regard, a recent study reported a positive correlation between Treg cell alongside CD8 T cell density in human CRC tumors and enhanced tumor control[15]. CRC is generally classified into two primary types based on the microsatellite stability status: 80-85% of CRC cases are characterized by stable microsatellite RNAs (microsatellite stable; MSS) and proficient mismatch repair mechanisms (mismatch repair proficient; MMRp); the remaining 15% exhibit microsatellite instability (microsatellite instability-high; MSI-H) and deficient mismatch repair mechanisms (mismatch repair deficient; MMRd). Although PD-1 blockade alone and in combination with CTLA-4 have recently shown impressive therapeutic responses in MSI-H CRC, MSS CRCs remain by and large resistant to these interventions[16,17]. Notably, one feature distinguishing the MSS CRC tumor microenvironment (TME) from the MSI-H one is the prevalence of regulatory T (Treg) cells in the former[15]. Mouse studies showed high degree of heterogeneity of colonic Treg cells, potentially stemming from their ontogeny[18-20], differentiation state, and specific effector features[21].

These effector features can contribute to different aspects of colon tissue biology as exemplified by terminally differentiated IL-10 expressing (IL-10^{+}) Treg cells preventing colon shortening[21]. Together, these observations raise a possibility that while in MSS CRC some tumoral Treg cells have an expected tumor-promoting function, a distinct subset of tumoral Treg cells may exert a seemingly incongruous anti-tumoral function by restraining activity of tumor-supportive accessory cells.

We tested this supposition by investigating the heterogeneity of transcriptional and chromatin states of tumoral vs. colonic Treg cells at a single cell resolution, using an orthotopic mouse model of MSS CRC that faithfully recapitulates human disease, as well as samples from human MSS CRC patients. Analysis of dynamic of tumoral Treg population during progression of tumors, established upon transplantation of *Apc*^{null}*Trp53*^{null} *Kras*^{G12D} cancer organoids[22], showed an enrichment in IL-10 non-expressing (IL-10^{-}) Treg cells over IL-10^{+} Treg cells, whereas the

exact opposite pattern was observed in the normal colon. Accordingly, targeted depletion of IL-10^{+} Treg cells increased the amounts of IL-17 produced by effector CD4 T cells, which by acting directly on CRC tumors promoted their growth, while selective loss of their IL-10^{-} counterparts resulted in a profound tumor shrinkage. Furthermore, the observed dichotomy between corresponding Treg subsets was conserved in human MSS CRC, where a higher prevalence of IL-10^{+} or IL-10^{-} Treg cells correlated with improved or worsened survival outcomes, respectively. Notably, meta-analysis of published single cell "omics" datasets identified Treg subsets with similar features in human lung and skin cancers. Together, our studies suggest that in MSS CRC and likely other barrier tissues malignancies, tumoral IL-10^{+} Treg cells exert an indirect antitumoral function within TME by suppressing production of tumor-supportive mediators, such IL-17, by other accessory cells including effector T cells. These findings offer a rationale for developing strategies for selective therapeutic targeting of distinct tumor-promoting – while sparing tumor-opposing – Treg cell subsets for immunotherapy of MSS CRC and other barrier epithelial tissue cancers.

RESULTS

AKP tumor is a faithful experimental model of human MSS CRC.

To investigate the heterogeneity and function of Treg cells in MSS CRC, we sought to employ an orthotopic mouse model of this cancer recapitulating properties of the human disease including CRC driver mutations, anatomic features of tumor growth, TME immune cell composition, prominent Treg cell presence and resistance to PD-1 blockade based therapy. Thus, we adopted orthotopic transplantation of mouse CRC stem cell organoids derived from intestinal stem cells with the induced hallmark mutations of human CRC: *Apc* and *Tp53* (p53) gene loss and oncogenic Kras^{G12D} expression[22](AKP). Tumors morphologically resembling human CRC protruded into the lumen and were macroscopically detectable at 2-4 weeks (Figure 1A) while spontaneous metastases were observed in the draining mesenteric lymph nodes (mLNs) and the

liver at 10 weeks after implantation of organoid cells into the cecal wall (Figure 1A, arrows). Notably, AKP TME showed overall significantly reduced immune cell presence with an enrichment in Treg cells and macrophages, and diminished effector CD8 T cell activity in comparison to hypermutated MC38 colon adenocarcinoma, a commonly used model of MSI CRC[23](Figure 1B-D) . The observed features distinguishing these orthotopic mouse model closely aligned with those of human CRCs (Figure S1)[24], highlighting the immunosuppressive character of the former[6]. Contrary to antibody-mediated PD-1 blockage sensitivity of MC38[25], AKP tumors were resistant to this therapeutic modality, which resulted in a mild increase in Treg cells with no significant changes in tumor volume or CD8 T cell activation status. This once again mirrored therapeutic response to PD-1 blockade and lack thereof in the corresponding human CRC types (Figures 1E-H). Together, these initial experiments established the AKP tumors as a faithful model of the human MSS CRC.

Multi-ome analyses identified heterogeneity within AKP associated Treg and effector T cells.

Considering that tumors regress upon Treg depletion in experimental mouse models and that human MSS CRC seems deviant from a typical association of tumoral Treg "richness" with poor prognosis, we investigated the efficacy of therapeutic Treg targeting in AKP tumor-bearing *Foxp3*^{DTR} mice, expressing diphtheria toxin receptor (DTR) under the control of the endogenous *Foxp3* locus. In keeping with the reported lack of a clear link between Treg cell abundance and clinical disease progression in human CRC patients, we found that the diphtheria toxin (DT)-induced pan-Treg depletion did not significantly alter tumor growth (Figure 1I). While these results appeared to suggest that Treg cell functionality is dispensable for AKP tumor progression, it remained possible that distinct subsets within tumoral Treg cell population may exert opposing effects on tumor growth resulting in a zero-sum effect.

To address this possibility and to further validate appropriateness of the AKP for studying human

disease we first examined heterogeneity of AKP tumor-associated Treg and effector T cell populations using paired single cell RNA/ATAC-seq analyses of highly purified T cell populations from the primary AKP tumors and adjacent tumor-free cecal tissue 4 weeks after transplantation. After processing, quality control filtering and clustering, 17 distinct clusters (15,621 cells) were identified based on the latent space representation of scRNA-seq data and visualized using uniform manifold approximation and projection (UMAP) (Figures 2A-2C). Analysis of the effector T cells showed that CD8 T cells encompassed four clusters containing terminally differentiated (*Pdcd1*^{hi} *Gzmb*^{lo}), effector (*Gzma*^{hi} *Gzmb*^{hi}), and memory (*Il7ra*^{hi} *Ccr7*^{hi}) CD8αβ T cells, and CD8αα T cells (Figure 2F). Effector CD4 T cells encompassed two Th1 (*Tbx21*$^{+}$ *Ifng*$^{+}$) alongside Th2 (*Gata3*$^{+}$ *Il4*$^{+}$ *Il5*$^{+}$), Th17 (*Rorc*$^{+}$ *Il17a*$^{+}$ *Il17f*$^{+}$), Tfh (*Cxcr5*$^{+}$ *Bcl6*$^{+}$), memory (*Ccr7*^{hi} *Sell*^{hi} *Il7ra*^{hi}), and recent draining LN emigrant (*S1pr1*^{hi}, CD4$_{NA}$) clusters (one each). Accordingly, analysis of motif accessibility in ATAC-seq peaks in each cluster showed enrichment of corresponding lineage-defining transcription factor motifs (T-box for Th1 and CD8; Sox for memory cells; Gata for Th2s; Rorc for Th17) (Figure 2D). In addition to these clusters containing both tumoral and colonic T cells, we identified two "tumor-only" clusters of highly activated PD-1^{+} Th1s and recently described innate-like FcεR1γ^{+} T cells (ILTCKs)[26] (Figure 2C and 2F). Of note, the effector T cell clusters identified in AKP tumors closely paralleled those observed in human MSS CRC[24], lending further support for the exactitude of this model of human disease.

Treg cells formed two clusters, which were annotated as IL-10^{+} and IL-10^{-} Treg cells based on their expression of the *Il10* gene. While these two clusters were populated by both colonic and tumoral cells, the majority of IL-10^{+} Treg cells were found in the cecum. In contrast, the IL-10^{-} Treg cells were enriched in the tumors raising a possibility of potentially distinct functions of IL10^{+} and IL10^{-} Treg cells in MSS CRC (Figure 2C). To gain insights into their dynamics during AKP tumor progression, we performed scRNA-seq of T cell populations from the tumor and adjacent cecal tissue at 2, 4, and 6 weeks after AKP organoid implantation. Extending the

observation of the tumoral Treg subset composition bias revealed by multiome analysis, the scRNA-seq time course, corroborated by flowcytometric analysis, showed a notable enrichment in IL-10^{-} to IL-10^{+} Treg cells with tumor progression while the relative size of IL-10^{+} Treg cells did not significantly change (Figure 2E, Figure S2B). The increase in IL-10^{-} Treg abundance was accompanied by a pronounced decline in tumor-specific PD-1^{+} CD4 T cells and PD1^{+} CD8 T cells, which were most abundant in "early" tumors at 2 weeks after implantation (Figure 2E and S2A). The observed increase in IL-10^{-} Treg cells aligns with their hypothesized tumor-promoting role, prompting further inquiry into the function of IL-10^{+} Treg cells. Notably, IL-10^{+} Treg cells were less abundant in AKP tumors compared to the cecum, and their relative proportion remained unchanged throughout tumor progression.

CRC-associated Treg cells diverge in gene regulatory programs.

The dynamics of IL-10^{+} and IL-10^{-} Treg cell subsets in CRC implied their distinct gene regulatory and transcriptional features. In this context, the former subset predominantly expressed *Rorc*, which encodes the transcription factor RORγt, whereas the latter expressed *Ikzf2* transcripts encoding Helios. Thus, RORγt^{+} and Helios^{+} Treg cells can serve as surrogates for the corresponding IL-10^{+} and IL-10^{-} Treg cell subsets (Fig. 3A). To further dissect their divergent transcriptional regulation, we employed the SCARlink algorithm to identify putative enhancers of signature genes for both populations using paired ATAC- and RNA-seq datasets[27]. Pseudo-bulk ATAC-seq tracks generated from the scATAC-seq data demonstrated differential accessibility between IL-10^{+} versus IL-10^{-} Treg cells at the putative enhancer sites in the *Foxp3*, *Il10*, and *Ikzf2* loci, reflecting their distinct transcriptional regulatory circuitry (Figure 3B). Consistently, the difference in number of gene-linked enhancers for some of the top differentially expressed genes closely correlated with the expression of the corresponding transcripts in these two subsets (Figure 3C).

To identify transcriptional modules expressed by IL-10^{+} versus IL-10^{-} Treg cells, we employed

Hotspot, a graph-based method of neighborhood analysis[28]. By calculating gene scores of the estimated modules, we identified modules unique to each annotated Treg subset that also displayed tumor- or cecum-specific patterns, indicating potential environmental imprinting of these regulatory programs (Figure 3D). Among the gene modules specific to IL-10^{-} but not IL-10^{+} Treg cells, two were enriched in cells residing in AKP tumors but not in adjacent cecal tissue. Henceforth referred to as the tumor IL-10^{-} Treg signature, these modules comprised *Ikzf2*, *Gata3*, and *Klrg1* transcripts in one, and *Zbtb46*, *Itgb8*, and *Il2ra* transcripts in the other. In contrast, the other IL-10^{-} Treg module with characteristic *Areg* and *Il10ra* expression, was preferentially detected in cells residing in the adjacent normal colonic tissue. The observed expression pattern likely reflected the heightened states of activation of tumoral IL-10^{-} Treg cells and the tissue-supporting function of their colonic counterparts. While two separable gene modules were also identified as IL-10^{+} Treg cell-specific, their expression did not vary between the tumor and adjacent normal cecum, indicating the lack of modulation of IL-10^{+} Treg cell transcriptional features by the CRC TME. These two IL-10^{+} Treg cell-specific modules were characterized by enrichment in *Il10, Maf, Ctla4, Ccr2*; as well as *Zeb2, Gzmb,* and *Il23r* transcript expression, respectively (Figure 3D). Analysis of the ATAC-seq data using chromVar showed that while tumor and colonic IL-10^{-} Treg cells shared certain TF binding motifs enriched at their unique accessible chromatin sites, the NR4A family motif was selectively enriched in tumoral IL-10^{-} Treg cells (Figure 3E). This result indicates a potentially stronger TCR signaling in the tumor-residing IL-10^{-} Treg cells, consistent with their heightened activation state implied by RNA-seq analysis (Figure 3D). In support of this notion, gene score analysis of tumoral versus cecal IL-10^{+} and IL-10^{-} Treg cells for TCR signaling and IL-2 signaling gene signatures showed the highest TCR signaling-related gene expression in tumoral IL-10^{-} Treg cells among all four subsets. In contrast, IL-10^{+} Treg cells showed the highest expression of IL-2 signaling related genes in accord with high *Il2ra* expression by these cells (Figure S3). Collectively, these results suggest potential functional divergence between IL-10^{+} and IL-10^{-} Treg in AKP tumor settings.

IL-10^{+} and IL-10^{-} Treg cells have opposing functions of in MSS CRC tumors.

To directly investigate the functionality of IL-10^{+} and IL-10^{-} Treg subsets in AKP we employed their punctual selective depletion using two complementary genetic tools recently developed in our laboratory. IL-10^{+} Treg cells were ablated upon DT administration into AKP bearing *Il10*$^{tdTomato\text{-}Cre}$ *Foxp3*$^{lsl\text{-}DTR}$ (*Il10*^{Cre}*Foxp3*$^{lsl\text{-}DTR}$) mice, in which Cre recombinase expressed under control of the *Il10* locus excised a STOP cassette preceding DTR coding sequence embedded into the *Foxp3* locus. Consequently, DTR is expressed exclusively in IL-10^{+} Treg cells in these mice. As a complementary approach, we induced selective DT-mediated ablation of IL-10^{-} Treg cells in AKP tumor-bearing *Il10*$^{tdTomato\text{-}Cre}$*Foxp3*$^{flox\text{-}DTR}$ (*Il10*^{Cre}*Foxp3*$^{flox\text{-}DTR}$) mice, in which *Il10* locus-driven Cre excised loxP sites-flanked DTR coding sequence from the *Foxp3* locus resulting in DTR expression exclusively in IL-10-non-expressing Treg cells. The experimental and control groups of mice were treated with DT or heat-inactivated (boiled DT; bDT), respectively, on day 1, 2, 5, 9, and 13 after intra-cecal implantation of AKP tumor organoid (Figure 4A). This resulted in efficient selective elimination of DTR-expressing Treg populations in *Il10*^{Cre}*Foxp3*$^{\mathrm{lsl\text{-}DTR}}$ and *Il10*^{Cre}*Foxp3*$^{\mathrm{flox\text{-}DTR}}$ mice (Figure S4A), as indicated by the depletion of tumoral RORγt^{+} and Helios^{+} Treg cells, respectively (Figures S4B-C). While these perturbations in the Treg cell subsets did not significantly alter overall immune cell infiltration of AKP tumors (Figure S4D), IL-10^{-} Treg cell depletion led to a marked reduction in the tumor sizes, which upon closer histological examination showed negligible remaining tumor cells accompanied by pronounced infiltration of mononuclear cells and increased tumoral CD8 T cell responses. This observation suggests efficient mobilization of anti-tumor effectors upon removal of IL-10^{-} Treg cells (Figure 4C, S4E, bottom panels). In contrast, depletion of IL-10^{+} Treg cells resulted in a notable increase in tumor sizes without detectable changes in effector CD8 or CD4 T cell numbers, suggesting the enhanced tumor growth was not a consequence of a diminished overall anti-tumoral T cell response, but potentially its altered “flavor” favoring tumor progression (Figure S4E, top panels).

To characterize potentially divergent effects of DT mediated depletion of these Treg cell subsets on the AKP TME, we first examined the myeloid populations in AKP tumors 2 weeks after installation of tumor organoids in *Il10*^{Cre}*Foxp3*$^{lsl\text{-}DTR}$ and *Il10*^{Cre}*Foxp3*$^{flox\text{-}DTR}$ mice. Ablation of IL-10^{+} Treg cells resulted in a significant increase in Ly6C^{hi} monocytes, macrophages, and neutrophils, but not mast cells or eosinophils indicative of a heightened type 3 response (Figure 5 and Figure S5A, top panels). Tumor-associated macrophages and neutrophils are known for their tumor-promoting functions in CRC[29-31]. In contrast, IL-10$^{–}$ Treg cell ablation following tumor inoculation resulted in decreased monocyte, macrophage, and neutrophil abundance, accompanied by a notable increase in eosinophils in the TME, potentially reflective of an increased type 2 response (Figure 5 and Figure S5A, bottom panels). Indeed, flow cytometric and RNA-seq analyses of tumoral effector CD4 T cell subsets after selective ablation of IL-10^{+} Treg cells showed a pronounced increase in expression of *Rorc*, the Th17 lineage defining TF, and type 3 cytokine IL-17 and IL-22 with concomitant decrease in type 2 cytokines IL-4 and IL-13, while granzyme B or IFNγ expression by CD8 T cells remained unchanged (Figure 6A-B, top panels; 6C and S5B). In a conspicuous contrast, depletion of IL-10$^{–}$ Treg cells led to an increase in IFNγ producing CD8 T cells and type 2 cytokine-producing CD4 T cells coupled with a decrease in IL-17 expressing Th17 cells (Figures 6A-B, bottom panels). Together, these data demonstrated that in AKP tumors IL-10^{+} Treg cells selectively repress Th17 responses, whereas IL-10$^{–}$ Treg cells specifically repress Th2 and CD8 T cell responses. Collectively, these results suggest that IL-10^{+} and IL-10$^{–}$ Treg cells regulate the CRC TME by modulating the "tone" of anti-tumor immune responses.

IL-10^{+} Treg cells oppose CRC progression by limiting IL-17 production

Previous studies implicated IL-17 signaling in promoting early stages of transformation of intestinal epithelial cells in addition to vascularization or recruitment of pro-tumoral myeloid cells[32-35]. Therefore, the increases in type 3 cytokines IL-17 and IL-22 and tumor sizes noted

upon depletion of IL-10^{+} Treg cells raised a possibility of a direct effect on IL-17 or IL-22 on AKP tumor cells. In support of this notion, we observed increased growth of AKP tumor organoids *in vitro* in the presence of IL-17, but not IL-22 (Figure 6D). Analysis of published bulk RNA-seq datasets revealed high *Il17ra* gene expression in similar mouse CRC organoids, lending further support for the idea that IL-17 may signal directly to AKP tumor cells to promote their proliferation[36]. To test this hypothesis, we generated IL17Rα-deficient AKP organoids using CRISPR-Cas9 mediated gene editing. Once transplanted into the cecum, the IL17Ra-deficient tumors were of significantly lower size than their control counterparts implicating direct signaling through IL-17Rα in their IL-17 dependent growth (Figure 6E). Because the enhanced tumor progression or its restraint caused by depletion of IL-10^{+} or IL-10$^{–}$ Treg cells, respectively, were also associated with the opposing effects on IL-4 and IL-13 production, we tested whether a decrease in these cytokines could have contributed to increased tumor growth in the absence of IL-10^{+} Treg cells. While antibody mediated neutralization of IL-4 and IL-13 resulted in a marked reduction in tumoral eosinophils and concomitant mild increase in tumoral neutrophils (Figure 6F), tumor sizes were unaffected in comparison to IgG isotype control treated group (Figure 6G). These data suggest that a decrease in type 2 cytokines does not contribute in a non-redundant manner to increased CRC tumor growth in the absence of IL-10^{+} Treg cells.

Previous studies showed that Th17 cells can be directly controlled through their IL-10R signaling in response to IL-10 produced by both Foxp3^{+} and Foxp3$^{–}$ CD4 T cells[37-39]. In light of these observations, our results suggest that the accelerated tumor growth caused by depletion of IL-10^{+} Treg cells was due to IL-17R signaling in AKP cells induced by increased IL-17 production when its restraint imposed by IL-10R signaling was relieved. To test this idea, we employed antibody-mediated blockade of IL-10Rα signaling in AKP tumor bearing mice. In corroboration of this supposition, IL-10Rα blockage resulted in an increase in IL-17 production by CD4 T cells and increased tumor sizes similar to those observed upon IL-10^{+} Treg cell

depletion (Figures 6H-I). Furthermore, IL-17Rα-deficient AKP tumors were insensitive to IL-10R blockade as their sizes were comparable to those in IgG isotype control-treated mice (Figure 6J). Taken together, our results suggest that while tumoral IL-10^{-} Treg cells expectedly promote CRC tumor progression, IL-10^{+} Treg cells restrain primary CRC tumors in an IL-10 signaling dependent manner. The latter limits production of IL-17, which acts directly on AKP carcinoma cells promoting their growth.

The duality of Treg populations is conserved in human CRC tumors.

We next asked whether IL-10^{+} vs IL-10^{-} Treg cell subsets were present in human MSS CRC. To address this question, we performed paired multi-omic scRNA/ATAC-seq analyses of total T cell populations isolated from surgically resected primary CRC tumors and matched normal adjacent colonic tissue (NATs) from 3 patients. Analysis of total 21,676 T cells, which formed 8 distinct clusters (Figures 7A-B and S6A; see Methods), showed Treg cells forming two clusters resembling mouse tumoral IL-10^{+} and IL-10^{-} Treg cells; one of these clusters preferentially expressed *IL10* and *RORC*, and the other *IKZF2* gene transcripts (Figures S6B-C). Similar to their differential abundance in normal tissue vs tumor in mice, the human IL-10^{+} Treg cells were enriched in NATs, while the IL-10^{-} Treg cells were enriched in tumor samples (Figure 7C). scATAC-seq data analysis using chromVar indicated similar TF motif enrichment patterns within chromatin accessible sites between corresponding mouse and human subsets, with the enrichment of *RORC* motif noted in IL-10^{+} Treg cells and *GATA* and *NR4A* motives in IL-10^{-} Treg cells (Figure 7D). To determine transcriptional similarity of human IL-10^{+} and IL-10^{-} Treg cells to their mouse counterparts we employed mouse Treg subset-specific gene modules (Figure 3D) and determined their expression in human Treg cells. Both subsets exhibited significant enrichment for gene modules identified in their mouse counterparts (Figure 7E). Consistently, Hotspot analysis identified subset-specific gene modules in human CRC-infiltrating Treg cells that were similar to their mouse counterparts. Notably, *IKZF2*, *GATA3*, *CCR8*, and *CADM1* were preferentially expressed by IL-10^{-} Treg cells, whereas *MAF* and *ZEB2* were preferentially

expressed by IL-10^{+} Treg cells. Together, these results demonstrated that transcriptional and chromatin states of human CRC Treg cell subsets resembled those of mouse IL-10^{+} and IL-10$^{–}$ Treg cells. Notably, our analysis of human CRC T cell datasets made publicly available by 10X Genomics also identified two tumor-infiltrating Treg cell subsets transcriptionally similar to the ones identified by our multi-omic analysis[40] (Figure S7A-E). The examination of the accompanying spatial transcriptomic (ST) datasets further corroborated observations made in our tissue dissociation-based analysis by demonstrating an enrichment in IL-10^{+} Treg cells in NATs, while IL-10$^{–}$ Treg cells were preferentially enriched in the tumor foci (Figure 6G and S7F and S7G). Of note, both Treg cell subsets seem to be preferentially localized to the tumor margins in proximity of cancer-associated fibroblasts (Figure S7F and S7G).

Considering the opposing function of IL-10^{+} and IL-10^{-} Treg subsets in tumor progression in mice, we next sought to investigate the potential association of their relative abundance in human CRC with clinical outcomes. We leveraged bulk RNA-seq datasets of surgical CRC samples from 102 patients and deconvolved these data using published scRNA-seq datasets for total CRC immune cells from 10X Genomics to infer relative abundances of the two Treg cell subsets[40] (see Methods). The patients were then segregated into a high abundance group (H) and a low abundance group (L) based on their relative expression of characteristic gene signatures for each tumoral Treg population. Consistent with the anti-tumoral role of IL-10^{+} Treg cells observed in mouse experiments, patients in the IL-10^{+} Treg high abundance group showed significantly better survival when compared to those in the corresponding low abundance group. Conversely, patients in IL-10$^{–}$ Treg high abundance group exhibited significantly worse survival than in low abundance group in agreement with the pro-tumoral function of this subset established in mice (Figure S7H).

Having demonstrated the pro- and anti-tumoral functions of IL-10^{+} and IL-10$^{–}$ Treg cells in mouse CRC and their association with better and worse human CRC prognosis, respectively, we

next sought to determine whether similar populations of Treg cells can be identified in other human cancer types. Published single cell atlas of T cells across 16 cancer types showed 7 distinct Treg cell clusters[41] (Figure S8A). Upon closer examination, we found that clusters C0, C1, and C4 exhibited low expression for both IL-10^{+} and IL-10^{-} Treg cell gene modules, indicating their relatively less differentiated or activated state. Clusters C2, C3, and C5 showed high-level expression of IL-10^{-} Treg cell gene modules, while cluster C6 expressed a higher level of IL-10^{+} Treg cell signature module (Figure S8B and C). Although these patterns were indicative of overall transcriptional similarity of cluster 2, 3 and 5 cells to IL-10^{-} Treg cells, C3 and C5 cells were enriched in basal cell carcinoma (BCC) and head and neck squamous cell carcinoma (HNSC), respectively, suggesting cancer type dependent prevalence of a particular IL-10^{-} Treg cell flavor (Figure S8D). Importantly, both C2 and C6 populations showed significant presence in BCC, CRC, HNSC, and stomach adenocarcinoma suggesting dichotomy of tumoral IL-10^{+} and IL-10^{-} Treg cells is common across different barrier tissue cancers (Figure S8D).

DISCUSSIONS

Since their initial characterization as the cell type principally responsible for negative regulation of immune responses to “self” and “non-self” in the secondary lymphoid organs, wide-ranging functions of Treg cells residing in non-lymphoid tissues have become increasingly appreciated. Treg cell contributions to tissue maintenance can be classified into two principal categories wherein Treg cells act either indirectly via suppression of tissue damaging inflammatory responses or directly through production of tissue differentiation, growth, and repair factors[2,42]. Both direct and indirect functions encompass numerous molecular mechanisms such as production of immunomodulatory cytokines including IL-10, consumption of IL-2, CTLA-4-assisted removal of CD80 and CD86 from dendritic cell surface, production of extracellular adenosine, acetylcholine, and epithelial growth factor family member amphiregulin

(Areg), and Notch activation through expression of Notch ligand Jagged1[2]. These mechanisms are mobilized through Treg cell recruitment, activation, proliferation, and differentiation in response to various stressors including malignant transformation and tumor growth. While Treg cell activity can counteract precancerous hyperplasia and early tumor initiation by suppressing frank- or para-inflammation—potentially increasing the mutational load—both direct and indirect mechanisms of Treg function are regarded as major contributors to tumor progression[5]. The former suppress cytotoxic and inflammatory responses of NK and tumor and self-antigen-specific T cells and act alongside cell-intrinsic mechanisms, foremost PD-1 signaling, to enforce their terminal differentiation and loss of pro-inflammatory function[43,44]. The latter may directly induce signaling in tumor cells promoting their growth and fitness[45]. Besides their association with progression of human cancers, increased numbers of activated Treg cells upon therapeutic PD-1 blockade and have been linked to both resistance and hyper-progression of cancers[46] providing rationale for a combined PD-1 blockade and Treg depletion therapy[11].

CRC is a notorious outlier in regard to the commonly accepted tumor-promoting function of Treg cells with the conflicting reports on the correlation or lack thereof between Treg cells abundance and human CRC prognosis[7-10,21] One potential explanation for this discrepancy contends that the previous analyses did not discriminate between Foxp3^{hi} Treg and Foxp3^{lo} effector T cell contributions to overall Foxp3 transcript amounts and that the high numbers of the latter in CRC tumors correlated with their microbial invasion and are linked to a better prognosis[10]. However, effector T cell activation aside, microbiota and dietary antigens serve first and foremost as major drivers of heterogeneity of colonic Treg cell population stemming from extrathymic differentiation of RORγt^{+} and, to lesser degree, Gata3^{+} Treg cells in addition to activation of Treg cells of thymic origin residing in the colon[18-20].

These findings motivated our investigation of intra-tumoral heterogeneity of Treg cells in colon cancer and its role in CRC progression. Our multi-modal single cell analyses demonstrated that

IL-10^{+} RORγt^{+} and IL-10^{-} Helios^{+} Treg cells represent two distinct subsets of Treg cells residing in in the TME of mouse and human CRC and corresponding tumor-free colon tissues. These subsets exhibited differential enrichment of gene expression signatures downstream of TCR and IL-2 receptor, two major signaling pathways required for Treg cell function[47-49]. While IL-2-dependent gene signature was enriched, TCR-dependent one was attenuated in tumoral IL-10^{+} Treg cells with the exact opposite trend observed for IL-10^{-} Treg cells. These findings are consistent with the previous observations that IL-2 signaling promotes IL-10 expression through upregulation of BLIMP1, whereas withdrawal from TCR signaling is linked to terminal differentiation of colonic IL-10-producing Treg subset[21,50-53].

In addition to their divergent transcriptomic and epigenomic features, opposing functions exerted by IL-10^{+} and IL-10^{-} Treg cells counteracting and promoting growth of CRC tumors, respectively, were revealed by selective ablation of individual subsets. This functional duality was consistent with the inversion in the relative abundance of these subsets in the tumor (% IL-10^{+} Treg < % IL-10^{-} Treg cells) in comparison to normal cecal tissue (% IL-10^{+} Treg > % IL-10^{-} Treg cells) observed in mice. Notably similar trend was revealed by our analysis of human CRC and adjacent normal tissue spatial transcriptomic datasets. This tumoral IL-10^{+} Treg dynamic could be due to progressively diminishing amounts of IL-2 resulting from increased consumption by Treg and diminished production by effector T cells as CRC tumors grow.

The seemingly paradoxical function of IL-10^{+} Treg cells was predominantly due to their ability to suppress production of IL-17 by Th17 cells. Previous studies implicated IL-10 as a non-redundant control mechanism of Th17 cells mediated directly through signaling via IL-10R these cells express[37]. Fittingly, Treg cells express the highest amount of IL-10 on a per cell basis among IL-10 expressing cell types and account for the majority of IL-10 expressing T cells in the colon[21]. In support of the above notion, antibody mediated blockade of IL-10R signaling resulted in a similar increase in both IL-17 production and enhancement of tumor growth. IL-17

is known to exert diverse effects on a wide range cell types at barrier and other tissues mobilizing microbial defenses through recruitment of neutrophils and monocytes and induction of antimicrobial peptides, promoting fibrosis via augmenting production of extracellular matrix components, and inducing adipose thermogenesis[54]. Expectedly, a boost in IL-17 production observed upon relief of Th17 cells from IL-10^{+} Treg cell-mediated suppression was associated with increases in tumor-associated neutrophils, monocytes, and macrophages, the three cells type previously linked to colon cancer progression[29-31]. While we have not formally excluded potential contribution of the latter to the observed enhanced tumor growth, we found that contrary to IL-17R-sufficient tumors, which grew bigger upon IL-10R blockage, the IL17R-deficient CRC size remained unaffected despite increased IL-17 production. While Th17 cells also exhibited increased expression of IL-22, an epithelial maintenance factor which has been implicated in promoting DSS and azomethane induced colon tumorigenesis[55], we found IL-22 signaling in AKP tumors dispensable for boosting their growth contrary to a non-redundant role of IL-17. Together, our results suggest that IL-10^{+} Treg cells restrain CRC progression by suppressing Th17 cells and thereby limiting amount of IL-17, which promotes AKP tumor cell growth.

The tumor-restraining activity of IL-10^{+} Treg cells was counterbalanced by tumor-promoting activity of IL-10^{-} Helios^{+} Treg cells, which was most likely linked to their superior ability to subdue tumoral CD8^{+} T cell responses. Although besides tumoral CD8 T cells, IL-10^{-}Treg cells also suppressed production of type 2 cytokines IL-4 and IL-13 by tumoral effector CD4 T cells and consequent recruitment of eosinophils to the TME, neutralization of these cytokines did not have any measurable effect on CRC growth. Notably, we identified two subclusters of mouse and human IL-10^{-} Treg cells, one of which was populated by IL-10^{-} Treg cells residing in both of tumor and normal tissue, whereas another encompassed almost exclusively tumoral Treg cells with the highest expression of activation markers including chemokine receptor CCR8. Previously, we and others have identified CCR8 as highly expressed by Treg cells across

different human cancers[4,56]. Subsequent studies revealed efficacy of CCR8 depleting antibody for Treg targeting as a monotherpay and in combinations with PD-1 or VEGF blockade or vaccination in mouse and human cancer models[57-59]. These results suggest that in CRC, CCR8 targeting based therapeutic strategies may relieve suppression of effector antitumoral T cell responses while preserving suppression of production of tumor promoting factors.

The relevance of the observed functional heterogeneity in our mouse studies to human MSS CRC is reflected in the association of an enrichment in gene expression signature of human counterparts of mouse anti-tumoral IL-10^{+} RORγt^{+} Treg cells and pro-tumoral IL-10^{-} Treg cells with a better and worse prognosis, respectively. Furthermore, our analysis of publicly available pan-cancer scRNA-seq datasets identified the counterparts of the two principal Treg cell subsets across other barrier tissue cancer types suggesting potential clinical implications of the observed Treg heterogeneity beyond CRC.

In conclusion, our studies suggest that IL-10^{-} Treg cells by suppressing CD8 T cell responses in the TME thereby facilitating, while IL-10^{+} Treg cells restrain tumor progression by repressing Th17 response and thus limiting the production of IL-17, a cytokine that directly drives CRC tumor cell proliferation. On a general note, the described Treg-mediated suppression of a production of tumor growth factor by another cellular component of TME represent a previously unappreciated means of regulation of cancer progression. The functional dichotomy of two major Treg cell subsets revealed by our studies of colorectal cancer offers rationale for an enhanced therapeutic strategy selectively targeting pro-tumoral Treg cell subset while sparing their anti-tumoral counterparts in across different barrier tissue cancer types harboring both Treg subsets.

Resource availability

Lead contact

Further information and requests for resources and reagents may be directed to and will be fulfilled by the lead contact, Alexander Y. Rudensky (rudenska@mskcc.org) and Christina S. Leslie (lesliec@mskcc.org).

Materials availability

All reagents and resources used in this study should be directed to the lead contact. All reagents will be available based on requesting the lead contact and completing a Materials Transfer Agreement.

Data and code availability

All sequencing datasets available on the GEO database with the following accession number:

ACKNOWLEDGMENTS

We thank the Memorial Sloan Kettering Integrated Genomics Core facility for performing all sequencing and the Single Cell Research Initiative for processing the scRNA-seq samples. We thank Dr. Scott Lowe for kindly providing us with the AKP tumor organoid. We thank Dr. Francisco Sanchez-Vega, Fan Wu, and Dr. Julio Garcia-Aguilar for providing us access to the bulk RNA-seq data from 102 patients. We thank Dr. We thank Dr. Chin-Tung Chen and Dr. Julio Garcia-Aguilar for their assistance in obtaining patient tumor and normal adjacent tissue samples. This work was supported by the NCI Cancer Center Support Grant P30 CA008748, NIH grant R01 AI034206 (A.Y.R.), and the Ludwig Center at the Memorial Sloan Kettering Cancer Center (A.Y.R.). A.Y.R. is an investigator with the Howard Hughes Medical Institute. X.H. was supported by the Irvington Postdoctoral Fellowship from Cancer Research Institute and the Basic and Translational Immunology Postdoctoral Award from Ludwig Center for Cancer Immunotherapy. The content is solely the responsibility of the authors and not necessarily

represent the official views of the NIH.

AUTHOR CONTRIBUTIONS

X.H., D.F., S.M., C.S.L., and A.Y.R. conceived the project. X.H. and D.F. designed, performed, and analyzed experiments with assistance from E.S.A., N.B.H., A.P.G., E.Y.W., J.N.F., V.L., A,V, and Q.J. S.M. and C.S.L. performed analysis of the single cell sequencing experiments. X.H. and A.Y.R. wrote the manuscript with input from D.F., S.M., and C.S.L.

DECLARATION OF INTERESTS

A.Y.R. is an SAB member and has equity in Sonoma Biotherapeutics, RAPT Therapeutics, Surface Oncology, and Vedanta Biosciences, and is an SAB member of BioInvent and a co-inventor or has IP licensed to Takeda that is unrelated to the content of the present study. The remaining authors declare no competing interests.

FIGURE LEGENDS

Figure 1. **Orthotopic AKP tumor organoid model of human MSS CRC.**

(**A**) Left: schematic of orthotopic AKP tumor organoid transplantation model; Right: representative images of primary and metastasized tumor at indicated time point. (**B-D**) The frequencies of indicated populations as measured by flow cytometric analysis of indicated tumors 2 weeks after transplantation; (**E**) tumor sizes at 2 weeks after indicated treatment; (**F**) the frequencies or absolute numbers of indicated populations in AKP tumors 2 weeks after indicated treatment. Data shown are pooled from 2-3 independent experiments.

Figure 2. Paired single cell RNA-seq and ATAC-seq analysis of CRC tumor associated T cells.

(**A-B**) Paired scRNA-seq and scATAC-seq analysis of T cells isolated from AKP tumor or adjacent cecal tissues 4 weeks after tumor inoculation. UMAP plots are shown for (**A**) cell type annotations and (**B**) tissue annotations (n=15,621 cells). (**C**) Bar graphs depicting the number of cells for each cell type and the proportions for each tissue. (**D**) chromVAR motif enrichment of scATAC-seq from the multi-ome across different subsets of T cells. (**E**) Changes in proportion of T cell subsets in tumor 2, 4, and 6 weeks after inoculation as determine by scRNA-seq (n=31,795 cells). (**F**) The expression of selected genes of interest in T cell subsets from AKP tumors 4 weeks after inoculation.

Figure 3. Heterogeneity of CRC tumoral Treg cells.

(**A**) UMAP plots depicting the expression of marker genes distinguishing IL10^{+} and IL10^{-} Treg cells. (**B**) Gene browser chromatin accessibility tracks for *Foxp3*, *Il10*, and *Ikzf2* gene loci for IL10^{+} and IL10^{-} Treg cells. (**C**) Numbers of putative enhancers (left) and log fold change in gene expression (right) for select genes for IL10^{+} and IL10^{-} Treg cells. (**D**) Heatmap depicting expression of gene modules identified across all Treg subsets split by cells from tumor and adjacent tumor-free cecum. (**E**) chromVAR analysis of differential motif enrichment for all Treg

cell subsets with the indicated tissue origins.

Figure 4. Targeted ablation of IL10^{+} or IL10^{-} Treg cells results in opposing effects on CRC tumor growth.

(**A**) The experimental design schematics of diphtheria toxin (DT) induced selectively ablation of IL10^{+} and IL10^{-} Treg cells using genetic mouse models. (**B)** Tumor sizes in DT- and control bDT-treated *Il10*$^{tdTomato\text{-}Cre}$ *Foxp3*$^{lsl\text{-}dtr}$ (left) and *Il10*$^{tdTomato\text{-}Cre}$ *Foxp3*$^{flox\text{-}dtr}$ mice (right) mice two weeks after AKP organoid implantation. Pooled data from two independent experiments are shown. (**C**) H&E staining of AKP tumors from indicated treatment groups. Images are representative of 3 independent experiments.

Figure 5. Contrasting shifts in myeloid cell composition of the CRC tumor microenvironment upon IL10^{+} or IL10^{-} Treg cell depletion.

(**A-C**) Flow cytometric analysis of the frequencies of monocytes (**A**), macrophages (**B**), and neutrophils (**C**) in AKP tumors from indicated treatment groups in *Il10*$^{tdTomato\text{-}Cre}$ *Foxp3*$^{lsl\text{-}dtr}$ (top) and *Il10*$^{tdTomato\text{-}Cre}$ *Foxp3*$^{flox\text{-}dtr}$ mice (bottom) two weeks after AKP organoid implantation. Pooled data from two independent experiments are shown.

Figure 6. IL10^{+} and IL10^{-} Treg cells exert anti-and pro-tumor functions through regulation of CD4 T cell responses.

(**A-B**) Flow cytometric analysis of the indicated cytokines production by PMA/ionomycine stimulated CD8 T cells (**A**) and CD4 T cells (**B**) isolated from AKP tumors from *Il10*$^{tdTomato\text{-}Cre}$ *Foxp3*$^{lsl\text{-}dtr}$ (top) and *Il10*$^{tdTomato\text{-}Cre}$ *Foxp3*$^{flox\text{-}dtr}$ mice (bottom) two weeks after their implantation. (**C**) Pseudo-bulk RNA-seq analysis of differential gene expression in tumoral CD4 T cells from DT vs control (bDT) treated *Il10*$^{tdTomato\text{-}Cre}$ *Foxp3*$^{lsl\text{-}dtr}$ mice two weeks after AKP organoid implantation. Key genes of interest are labeled. (**D**) Frequencies and absolute numbers of CD8 and CD4 T cell numbers producing indicated effector molecules. (**E**) Weights of *Il17r*-sufficient

(WT) and -deficient (KO) AKP tumors two weeks after their implantation into C57BL/6 mice. (**F-I**) Flow cytometric analysis of the indicated cell types (**F, H**) and tumor weights (**G, I**) two weeks after the indicated treatments; for (**F)** and **(G)**, Tx: IL-4 and IL-13 neutralizing antibodies; Ctrl: isotype control IgG; for (**H)** and **(I)**, Tx: IL-10Rα blocking antibody; Ctrl: isotype control IgG. (**J**) Weights of *Il17r*-sufficient (WT) and -deficient (KO) AKP tumors two weeks after their implantation into C57BL/6 mice and indicated treatments (Ctrl, isotype control antibody injection; Tx, IL-10Rα blocking antibodies injection). Pooled data from two independent experiments are shown in all panels.

Figure 7. The IL10$^+$ and IL10$^-$ Treg cell subsets are present in human CRC.

(**A**) Paired scRNA-seq and scATAC-seq analysis of T cells isolated from surgical samples of tumors and normal adjacent colon tissues (NATs) of 3 CRC patients. UMAP plots are shown for cell type annotations (left) and tissue annotations (right) for n=21,676 cells. (**B**) Bar graph depicting the number of cells for each cell type. (**C**) Proportions of IL10$^+$ and IL10$^-$ Treg cells in tumor and NAT. (**D**) chromVAR analysis of differential motif enrichment within scATAC-seq peaks across different subsets of T cells. (**E**) Gene scores calculated on the cells from human multi-ome using the gene modules identified from mouse multi-ome for IL10$^+$ and IL10$^-$ Treg cells in Figure 3D. (**F**) Heatmap depicting gene expression of gene modules identified across all Treg cells in tumors from CRC patients. (**G**) Probabilistic prediction of IL10$^+$ Treg cells (left) and IL10$^-$ Treg cells (right) in 10x VisiumHD spatial data from CRC tumor and NAT[40].

Supplementary Figure 1. Distinct immune cell composition of human MMRd and MMRp CRC tumors.

Reanalysis of scRNA-seq CRC datasets from Pelka et al[24]. (**A**) Fraction of Tregs across patient samples grouped by MMRd and MMRp CRC. (**B**) Fraction of macrophage grouped by MMRd and MMRp CRC. (**C**) Differential *GZMB* and (**D**) *IFNG* expression in MMRd and MMRp CRC.

Supplementary Figure 2. Heterogeneities in T cells over time in tumor and adjacent cecum.

(**A**) Dynamics of T cell subsets in tumor and adjacent cecum at 2, 4, and 6 weeks after AKP organoid implantation based on scRNA+TCR-seq analysis (n=31,795 cells). (**B**) Flow cytometric analysis of the frequencies of RORγt^{+} and Helios^{+} Treg cell subsets in tumor and adjacent normal tissue at the indicated time points after AKP tumor implantation. Pooled data from two independent experiments are shown.

Supplementary Figure 3. TCR and IL-2 dependent gene expression in tumoral IL-10^{+} and IL-10^{-} Treg cell subsets.

Violin plots of gene scores of genes associated with IL-2 signaling (n=30 genes) and TCR-signaling (n=30 genes).

Supplementary Figure 4. Selective ablation of IL10^{+} and IL10$^{–}$ Treg cells does not result in significant changes in total immune cell infiltration or overall CD8 and CD4 T cell compositions.

(**A-E**) Flow cytometric analysis of the frequencies and absolute numbers of indicated tumoral populations in tumor in DT and control (Ctrl) bDT-treated *Il10*$^{tdTomato\text{-}Cre}$ *Foxp3*$^{lsl\text{-}dtr}$ (top) and *Il10*$^{tdTomato\text{-}Cre}$ *Foxp3*$^{flox\text{-}dtr}$ mice (bottom). Pooled data from two independent experiments are shown.

Supplementary Figure 5 Selective IL10^{+} and IL10$^{–}$ Treg cell loss results in distinct changes resulted in myeloid cell and CD4 T cell composition of the AKP tumor microenvironment.

(**A**) Flow cytometric analysis of mast cells and eosinophils two weeks in DT- and control (Ctrl) bDT-treated *Il10*$^{tdTomato\text{-}Cre}$ *Foxp3*$^{lsl\text{-}dtr}$ (top) and *Il10*$^{tdTomato\text{-}Cre}$ *Foxp3*$^{flox\text{-}dtr}$ mice (bottom). Pooled data from two independent experiments are shown. (**B**) *Il22* expression as measured by scRNA-seq analysis in indicated cell populations from mice.

Supplementary Figure 6. Single cell multi-ome analysis of T cells in from human CRC samples.

(**A**) Proportions of T cell subsets grouped by tissue (left) and by patients (right). (**B**) Expression of marker genes differentiating IL10^{+} and IL10^{-} Treg cells. (**C**) Dot plot of marker genes for T cell subsets.

Supplementary Figure 7. Single-cell flex and spatial data from 10x Genomics and survival analysis on bulk RNA. (**A**) UMAP of T cell subsets (n=18,198 cells) identified in single-cell flex data. (**B**) Bar graphs depicting the number of cells for each cell type and the proportions for each tissue (cecum/tumor). (**C**) Expression of *FOXP3* to highlight the Tregs. (**D**) Marker genes of T cell subsets. (**E**) Violin plots of gene scores calculated on the cells from single-cell flex using gene modules identified from mouse multi-ome for IL10^{+} and IL10^{-} Treg cells in Fig. 3D. (**F**) Predictions of cell types in spatial 10x VisiumHD. The single-cell flex data was used as reference. (**G**) Spatial plots highlighting the predictions of IL10^{+} and IL10^{-} Treg cells in tumor and NAT. (**H**) Bulk RNA-seq from CRC patients (n=102) deconvolved into cell types from single-cell flex. Kaplan-Meier survival curves using quantile cutoffs on the prediction proportions of IL10^{-} (left) and IL10^{+} Tregs (right).

Supplementary Figure 8. Pan-cancer analysis of human IL-10^{+} and IL-10^{-} Treg cell subsets.

(**A**) UMAP visualization of previously identified Treg clusters from 14 cancer types, metastases, adjacent healthy tissue, and cells from PBMC, bone marrow, and lymph node from healthy donors (n=30,031 cells)[41]. (**B**) Gene scores of modules identified for IL10^{+} and IL10^{-} Tregs from CRC patient samples in Fig. 7F. (**C**) Markers of select genes differentiating the Treg clusters. (D) Composition of the Treg subsets across 14 cancer types.

METHODS

Mice

Foxp3^{DTR}, *Il10*$^{tdTomato\text{-}Cre}$ *Foxp3*$^{lsl\text{-}DTR}$, and *Foxp3*$^{flox\text{-}DTR}$ mice have been previously described and maintained in house[21,60,61]. *Il10*$^{tdTomato\text{-}Cre}$ *Foxp3*$^{flox\text{-}dtr}$ mice were generated by intercrossing the two strains to homozygosity for each allele. Littermates were used in all experiments and were distributed among experimental groups evenly whenever possible, with different experimental groups co-housed. In experiments with different genotypes, all genotypes were represented in each litter analyzed. All mice were housed at the Research Animal Resource Center for Memorial Sloan Kettering Cancer Center and Weill Cornell Medicine. All studies were under protocol 08-10-023 and approved by the Sloan Kettering Institute Institutional Animal Care and Use Committee. All animals used in this study had no previous history of experimentation and were naive at the time of analysis.

AKP tumor inoculation

AKP tumor organoid are maintained as previously described[22]. For each experiment, tumor organoid 3D culture is digested with TrypLE and resuspend at the density of 12,500,000 cells/ml in PBS:Geltrex (2:1) mixture and maintained on ice, 20ul of the cell suspension is injected into the subserosa space of mouse cecum.

AKP tumor *in vitro* cytokine treatment

AKP tumor organoid are cultured *in vitro* as previously described[22]. On day 1, cells were seeded at 0.67 million cells/ml in PBS:Geltrex (1:2) mixture and plated into 40ul droplets at 1 drop per well concentration in a 24 well plate. Cells were treated with IL-17a and IL-22 at a concentration of 50ng/ml each on day 1 and day 3. Cells from each well are harvested and counted on day 7.

Gene editing of AKP tumor organoid

AKP organoids were electroporated using previously described protocol[62]. 2μg of *in vitro* transcribed Cas9 mRNA, 200 pmol of sgRNAs (5': GTGTTGATTACCGATGAGAA; 3': GCAGCTAATCACCCCTAAGG) each, and 2μg of linearized donor plasmid were used per electroporation. Donor plasmids were designed with 40bp homology arms flanking both sgRNA cut sites. A targeting construct consisted of a EF1α promoter driving the Thy1.1 coding sequence, followed by a STOP codon, and polyA sequence was inserted into the *Il17ra* locus by Microhomology-mediated end joining. The success of knock-in was verified with genotyping PCR (Il17ra-F: GACTACTTGGCAGCAGAGCA; Il17ra-R: GCCAAGCCAGCACCACTG; EF1a-R: ACTTTCCCAGTTTACCCCGC) and flowcytometric analysis of Thy1.1 expression. Organoid cells were sorted on Thy1.1 positivity twice before inoculation. For control organoid, only Cas9 RNA was used for the electroporation process.

Mouse treatments

For diptheria toxin (DT) treatment, DT was reconstituted in sterile PBS at 1 mg/ml and frozen at –80°C in single use aliquots. Aliquots were thawed and diluted in 995 μL PBS. For inactivated control (bDT), this 1 mL dilution was heated at 95 – 100°C for 30 minutes. Both active and control DT were filtered through 0.22 μm syringe-driven filters. Mice were injected intravenously with 200 μL of this dilution for the first doses (1000 ng DT) and 200 μL of a 1:1 dilution with PBS for the second dose (500 ng DT) or intraperitoneally with 200 μL of a 1:1 dilution with PBS for the second dose for subsequent doses (500 ng DT).

For antibody treatment in tumor-bearing mice, the first dose immediately after the surgery was given by retroorbital *i.v.* injection, while all the subsequent injections were given *i.p.* Anti-PD1 antibody was injected on day 1, 4, 7, 10, and 13 at a dosage of 0.5mg/mouse in 200ul of saline. Anti-IL-10Rα antibody was injected on day 1 and day 8 after surgery at a dosage of 1mg/mouse in 100ul of saline. Anti-IL-4 and anti-IL-13 antibodies were injected on day 1, 4, 7, 10, and 13 at a dosage of 50ng/mouse each in 200ul of saline.

Cell isolation for flow cytometry

Mice were injected retro-orbitally with 1.5 µg anti-mouse CD45.2 (Brilliant Violet 510 conjugated, BioLegend 109838) in 200 µL sterile PBS 3 min prior to euthanasia to label and exclude blood-exposed cells. All centrifugations were performed at 700x g for 3 min at 4 °C. Secondary lymphoid organs were dissected and placed in 1 mL wash medium (RPMI 1640, 2% Fetal Bovine Serum (FBS), 10 mM HEPES buffer, 1% penicillin/streptomycin, 2 mM L-glutamine). Tissues were then mechanically disrupted with the back end of a syringe plunger, and then passed through a 100 µm, 44% open area nylon mesh. For tumor and cecum, the cecal pouch was dissected, and after removal of fat and the cecal patch, opened longitudinally and vigorously shaken in 1x PBS to remove luminal contents. Tumor was then dissected from the surrounding cecal tissue. Both tumor and cecum were placed in a 50 mL screw-cap tube with 25 mL wash medium supplemented with 5 mM EDTA and 1 mM dithiothreitol and shaken horizontally at 250 RPM for 15 to 20 min at 37°C. After a 5 sec vortex, epithelial and immune cells from the epithelial layer were removed by filtering the suspension through a tea strainer. Remaining tissue was placed back in 50 mL tubes, washed with 25 mL wash medium, strained again, and replaced in 5 mL tubes. Tumor was minced into pieces with the size of approximately 1-2mm diameters. 25 mL wash medium supplemented with 0.2 U/mL collagenase A, 4.8 mM calcium chloride, 1 U/mL DNase I was added, along with four ¾ inch ceramic beads, and tissues were shaken horizontally at 250 RPM for 35 min at 37°C. Suspension was then passed through a 100 µm strainer, centrifuged to remove debris and collagenase solution, and then washed by centrifugation in 40% PercollTM in wash medium. All enzymatically digested samples were washed by centrifugation in 5 mL wash medium.

Flow cytometry

To assess cytokine production after ex vivo restimulation, single cell suspensions were incubated for 4 hours at 37°C with 5% CO2 in the presence of 50 ng/mL PMA and 500 ng/mL ionomycin with 1 µg/mL brefeldin A and 2 µM monensin to inhibit ER and Golgi transport. For flow

cytometric analysis, cells were stained in 96 well V-bottom plates. All centrifugations were performed at 700x g for 4 min at 4 °C for live cells and 900x g for 2 min for fixed cells. Staining with primary antibodies was carried out in 100 µL for 25 min at 4°C in staining buffer (PBS, 0.2 % (w/v) BSA, 2 mM EDTA, 10 mM HEPES, 0.1% (w/v) NaN3). Cells were then washed with 200 µL PBS and then concurrently stained with Zombie NIR™ Fixable Viability dye and treated with 20 U/mL DNase I in DNase buffer (2.5 mM MgSO4, 0.5 mM CaCl2, 136.9 mM NaCl, 0.18 mM Na2HPO4, 5.36 mM KCl, 0.44 mM KH2PO4, 25 mM HEPES) for 10 min at room temperature. Cells were washed with 100 µL staining buffer, resuspended in 200 µL staining buffer, and passed through a 100 µm nylon mesh. For cytokine staining, cells were fixed and permeabilized with BD Cytofix/Cytoperm per manufacturer instructions. Intracellular antigens were stained overnight hour at 4°C in the 1x Perm/Wash buffer. Samples were then washed twice in 200 µL 1x Perm/Wash buffer, resuspending each time, resuspended in 200 µL staining buffer, and passed through a 100 µm nylon mesh. All samples were acquired on an Aurora cytometer (Cytek Biosciences) and analyzed using FlowJo v10 (BD Biosciences).

Cell sorting for sequencing

For mouse samples, cell isolation was performed as described above, except that samples were not washed with 40% PercollTM. Staining was performed as described above, except buffer contained 2 mM L-glutamine and did not contain NaN3, with staining volume adjusted to 500 µL and washes adjusted to 5 mL and staining performed in 15 mL screw-cap tubes. 1 µg 'HashTag' antibodies (BioLegend, 155801, 155803, 155805, 155807) were added to extracellular antigen stain for scRNA-seq sorting, and scRNA-seq sort samples were not DNase I treated. Samples were resuspended in Wash buffer supplemented 5mM EDTA for sorting and sorted into wash medium in 1.5 mL Protein LoBind tubes. For human CRC tissues, samples were weighed and dissociated with Tumor Dissociation Kit, Human (Miltenyi Biotec) on a gentleMACS^{TM} dissociator (Miltenyi Biotec) using programs recommended for CRC samples.

Suspension was then passed through a 100 μm strainer, centrifuged to remove debris and collagenase solution, and then washed by centrifugation in RPMI extensively.
All sorting was performed on an Aria II (BD Biosciences) or an AuroraCS cytometer (Cytek Biosciences).

Histological analysis

The entire tumor tissue with ~0.5cm of surrounding cecal tissue were fixed in 4% PFA for > 48 hours. Tissue embedding, sectioning, and staining was carried out by the Molecular Cytology Core at MSKCC.

Single cell sequencing data preprocessing

The FASTQ files from all the single cell datasets were aligned using the Cell Ranger pipeline. We performed quality control and applied different filtering thresholds for each dataset. For the mouse scRNA-seq data from the single-cell multi-ome of RNA+ATAC at 4 weeks, we restricted the percentage of mitochondrial reads (pct_counts_mt) to less than 10%, the number of genes expressed in each cell (n_genes_by_counts) to a maximum of 3,000, and the UMI counts (total_counts) to at least 1,000. For the scATAC-seq data from the same multi-ome, we retained cells with at least 180 fragments and a TSS enrichment score of at least 3. The TSS enrichment score is the ratio of the number of reads at the gene TSS relative to the flanking regions[63]. For the mouse scRNA-seq data from 2, 4, and 6 weeks, we retained cells with pct_counts_mt less than 20%, n_genes_by_counts at most 3,000, and total_counts at least 500. In case of the metastasis scRNA-seq data from 10 weeks, we retained cells with pct_counts_mt less than 7%, n_genes_by_counts less than 4,200, and total_counts greater than 500. Finally, for the scRNA-seq from the multi-ome of patient samples, we extracted cells with pct_counts_mt less than 20%, n_genes_by_counts greater than 800, and total_counts less than 6,000. The matched scATAC-seq data from the patient samples were filtered to retain cells with at least 1,000 fragments and a

TSS enrichment score of at least 4. For the multi-ome data sets, we retained the cells that passed quality control (QC) thresholds in both scRNA-seq and scATAC-seq.

Batch correction and cell-type annotation

The single cell multi-ome of the patient samples had strong batch effects in both scRNA-seq and scATAC-seq. To this end, we used combat[64,65] on the log-normalized counts from scRNA-seq to generate batch-corrected counts. Using the batch-corrected counts, we performed principal component analysis (PCA) that we used to generate a UMAP embedding for visualization. We ran CellSpace[66] on the top 25,000 variably accessible 500bp tiles with the margin parameter set to 0.1 to generate a batch corrected latent space embedding of the scATAC-seq data. This latent space embedding was used to generate a UMAP embedding for visualization. All the other remaining data sets did not have batch effects. In those cases, we performed dimensionality reduction using PCA on the normalized scRNA-seq counts and iterative LSI[63] on the scATAC-seq tiles followed by UMAP generation.

We performed Leiden clustering on the PCA components of scRNA-seq for all the data sets. The clustering was performed in an iterative manner where we sub-clustered specific clusters to obtain clearer signal of specific phenotypes. The cluster labels were transferred to scATAC-seq data for chromatin accessibility-based analyses.

Transcription factor binding activity analysis

We called peaks in the scATAC-seq data sets using Macs2[67] by grouping the cells into pseudo-bulks based on the cell-type annotations obtained from matched scRNA-seq. Then, we ran chromVAR[68] on these peak sets to quantify the enrichment of TF binding sites in the accessible regions of individual cells.

Prediction of regulatory regions from single-cell multi-ome

We ran SCARlink[27] on the subsets of CD4 T cells from the single cell mouse multi-ome. We trained models on 4,315 genes that are highly variable and that have transcripts in at least 10% of all the CD4 T cells. We extracted the predicted gene-linked enhancer tiles with z-score greater than 0.5 and false discovery rate (FDR) of 0.05 to compare the number of gene-specific enhancers predicted for $IL10^+$ and $IL10^-$ Tregs.

Identification of gene modules

We used Hotspot[28] separately on mouse and human scRNA-seq data to identify gene modules for Tregs. To this end, we first filtered out cells that were not Tregs and genes that were not expressed in any of the Treg cells. We also filtered out Malat1/MALAT1, mitochondrial genes, and ribosomal genes. We generated k-nearest neighbor (kNN) graphs with 30 neighboring cells. For the mouse data, we generated modules with at least 25 genes at FDR < 0.05 and for the human analysis, we generated modules with at least 35 genes at FDR < 0.0001. This gave us seven gene modules in the mouse data and five gene modules in the human data. The gene scores calculated using these gene modules were generated using the score_genes() function from scanpy[65].

Analysis of single-cell flex data from 10x genomics

We first extracted the Cell Ranger processed output to retain cells with mitochondrial read percentage of less than 25% and UMI counts greater than 500. Then we log-normalized the count matrix and performed PCA on the top 2,000 highly variable genes. We performed Leiden clustering to obtain the broad cell type categories. We then extracted the T cells and re-clustered the cells to identify granular cell populations.

Analysis of VisiumHD data from 10x genomics

We analyzed the VisiumHD data sets at 8 µm resolution. We first filtered and retained spots with mitochondrial reads percentage less than 25%, and UMI counts greater than 500. We then used

Tacco[69] to annotate the cell types in the Visium HD samples using the single-cell Flex data as reference. Since we have matched samples in both Flex and Visium, we used the identifical sample in Flex as reference, when performing the label transfer. We used the annotate() function in TACCO with parameters multi_center=3 and lamb=1e-3.

Survival analysis

We ran BayesPrism[70] to deconvolve the bulk RNA-seq data sets using the single-cell flex as reference. This generated probabilistic predictions of deconvolution for each cell type in the reference atlas. We applied quantile cutoffs on the probabilistic predictions of $IL10^{+}$ and $IL10^{-}$ Tregs and generated Kaplan-Meier survival plots.

REFERENCES:

1. Josefowicz, S.Z., Lu, L.F., and Rudensky, A.Y. (2012). Regulatory T cells: mechanisms of differentiation and function. Annu Rev Immunol *30*, 531-564. 10.1146/annurev.immunol.25.022106.141623.
2. Dikiy, S., and Rudensky, A.Y. (2023). Principles of regulatory T cell function. Immunity *56*, 240-255. 10.1016/j.immuni.2023.01.004.
3. Huang, X., and Rudensky, A.Y. (2024). Regulatory T cells in the context: deciphering the dynamic interplay with the tissue environment. Curr Opin Immunol *89*, 102453. 10.1016/j.coi.2024.102453.
4. Plitas, G., Konopacki, C., Wu, K., Bos, P.D., Morrow, M., Putintseva, E.V., Chudakov, D.M., and Rudensky, A.Y. (2016). Regulatory T Cells Exhibit Distinct Features in Human Breast Cancer. Immunity *45*, 1122-1134. 10.1016/j.immuni.2016.10.032.
5. Plitas, G., and Rudensky, A.Y. (2020). Regulatory T Cells in Cancer. Annual Review of Cancer Biology *4*, 459-477. 10.1146/annurev-cancerbio-030419-033428.
6. Frey, D.M., Droeser, R.A., Viehl, C.T., Zlobec, I., Lugli, A., Zingg, U., Oertli, D., Kettelhack, C., Terracciano, L., and Tornillo, L. (2010). High frequency of tumor-infiltrating FOXP3(+) regulatory T cells predicts improved survival in mismatch repair-proficient colorectal cancer patients. Int J Cancer *126*, 2635-2643. 10.1002/ijc.24989.
7. Miyara, M., Yoshioka, Y., Kitoh, A., Shima, T., Wing, K., Niwa, A., Parizot, C., Taflin, C., Heike, T., Valeyre, D., et al. (2009). Functional delineation and differentiation dynamics of human CD4+ T cells expressing the FoxP3 transcription factor. Immunity *30*, 899-911. 10.1016/j.immuni.2009.03.019.
8. Sinicrope, F.A., Rego, R.L., Ansell, S.M., Knutson, K.L., Foster, N.R., and Sargent, D.J. (2009). Intraepithelial effector (CD3+)/regulatory (FoxP3+) T-cell ratio predicts a clinical outcome of human colon carcinoma. Gastroenterology *137*, 1270-1279. 10.1053/j.gastro.2009.06.053.
9. Salama, P., Phillips, M., Grieu, F., Morris, M., Zeps, N., Joseph, D., Platell, C., and Iacopetta, B. (2009). Tumor-infiltrating FOXP3+ T regulatory cells show strong prognostic significance in colorectal cancer. J Clin Oncol *27*, 186-192. 10.1200/JCO.2008.18.7229.
10. Saito, T., Nishikawa, H., Wada, H., Nagano, Y., Sugiyama, D., Atarashi, K., Maeda, Y., Hamaguchi, M., Ohkura, N., Sato, E., et al. (2016). Two FOXP3(+)CD4(+) T cell subpopulations distinctly control the prognosis of colorectal cancers. Nat Med *22*, 679-684. 10.1038/nm.4086.
11. Arce Vargas, F., Furness, A.J.S., Solomon, I., Joshi, K., Mekkaoui, L., Lesko, M.H., Miranda Rota, E., Dahan, R., Georgiou, A., Sledzinska, A., et al. (2017). Fc-Optimized Anti-CD25 Depletes Tumor-Infiltrating Regulatory T Cells and Synergizes with PD-1 Blockade to Eradicate Established Tumors. Immunity *46*, 577-586. 10.1016/j.immuni.2017.03.013.
12. van Gulijk, M., van Krimpen, A., Schetters, S., Eterman, M., van Elsas, M., Mankor, J., Klaase, L., de Bruijn, M., van Nimwegen, M., van Tienhoven, T., et al. (2023). PD-L1 checkpoint blockade promotes regulatory T cell activity that underlies therapy resistance. Sci Immunol *8*, eabn6173. 10.1126/sciimmunol.abn6173.
13. Sledzinska, A., Vila de Mucha, M., Bergerhoff, K., Hotblack, A., Demane, D.F., Ghorani, E., Akarca, A.U., Marzolini, M.A.V., Solomon, I., Vargas, F.A., et al. (2020). Regulatory T Cells Restrain Interleukin-2- and Blimp-1-Dependent Acquisition of

Cytotoxic Function by CD4(+) T Cells. Immunity *52*, 151-166 e156. 10.1016/j.immuni.2019.12.007.
14. Society, A.C. (2024). Cancer Facts & Figures 2024.
15. Frei, A.L., McGuigan, A., Sinha, R., Jabbar, F., Gneo, L., Tomasevic, T., Harkin, A., Iveson, T., Saunders, M.P., Oien, K.A., et al. (2024). Multiplex analysis of intratumoural immune infiltrate and prognosis in patients with stage II-III colorectal cancer from the SCOT and QUASAR 2 trials: a retrospective analysis. Lancet Oncol *25*, 198-211. 10.1016/S1470-2045(23)00560-0.
16. Le, D.T., Uram, J.N., Wang, H., Bartlett, B.R., Kemberling, H., Eyring, A.D., Skora, A.D., Luber, B.S., Azad, N.S., Laheru, D., et al. (2015). PD-1 Blockade in Tumors with Mismatch-Repair Deficiency. N Engl J Med *372*, 2509-2520. 10.1056/NEJMoa1500596.
17. Andre, T., Elez, E., Van Cutsem, E., Jensen, L.H., Bennouna, J., Mendez, G., Schenker, M., de la Fouchardiere, C., Limon, M.L., Yoshino, T., et al. (2024). Nivolumab plus Ipilimumab in Microsatellite-Instability-High Metastatic Colorectal Cancer. N Engl J Med *391*, 2014-2026. 10.1056/NEJMoa2402141.
18. Sefik, E., Geva-Zatorsky, N., Oh, S., Konnikova, L., Zemmour, D., McGuire, A.M., Burzyn, D., Ortiz-Lopez, A., Lobera, M., Yang, J., et al. (2015). MUCOSAL IMMUNOLOGY. Individual intestinal symbionts induce a distinct population of RORgamma(+) regulatory T cells. Science *349*, 993-997. 10.1126/science.aaa9420.
19. Ohnmacht, C., Park, J.H., Cording, S., Wing, J.B., Atarashi, K., Obata, Y., Gaboriau-Routhiau, V., Marques, R., Dulauroy, S., Fedoseeva, M., et al. (2015). MUCOSAL IMMUNOLOGY. The microbiota regulates type 2 immunity through RORgammat(+) T cells. Science *349*, 989-993. 10.1126/science.aac4263.
20. Kim, K.S., Hong, S.W., Han, D., Yi, J., Jung, J., Yang, B.G., Lee, J.Y., Lee, M., and Surh, C.D. (2016). Dietary antigens limit mucosal immunity by inducing regulatory T cells in the small intestine. Science *351*, 858-863. 10.1126/science.aac5560.
21. Dikiy, S., Ghelani, A.P., Levine, A.G., Martis, S., Giovanelli, P., Wang, Z.M., Beroshvili, G., Pritykin, Y., Krishna, C., Huang, X., et al. (2025). Terminal differentiation and persistence of effector regulatory T cells essential for preventing intestinal inflammation. Nat Immunol. 10.1038/s41590-024-02075-6.
22. O'Rourke, K.P., Loizou, E., Livshits, G., Schatoff, E.M., Baslan, T., Manchado, E., Simon, J., Romesser, P.B., Leach, B., Han, T., et al. (2017). Transplantation of engineered organoids enables rapid generation of metastatic mouse models of colorectal cancer. Nat Biotechnol *35*, 577-582. 10.1038/nbt.3837.
23. Efremova, M., Rieder, D., Klepsch, V., Charoentong, P., Finotello, F., Hackl, H., Hermann-Kleiter, N., Lower, M., Baier, G., Krogsdam, A., and Trajanoski, Z. (2018). Targeting immune checkpoints potentiates immunoediting and changes the dynamics of tumor evolution. Nat Commun *9*, 32. 10.1038/s41467-017-02424-0.
24. Pelka, K., Hofree, M., Chen, J.H., Sarkizova, S., Pirl, J.D., Jorgji, V., Bejnood, A., Dionne, D., Ge, W.H., Xu, K.H., et al. (2021). Spatially organized multicellular immune hubs in human colorectal cancer. Cell *184*, 4734-4752 e4720. 10.1016/j.cell.2021.08.003.
25. Wei, S.C., Anang, N.A.S., Sharma, R., Andrews, M.C., Reuben, A., Levine, J.H., Cogdill, A.P., Mancuso, J.J., Wargo, J.A., Pe'er, D., and Allison, J.P. (2019). Combination anti-CTLA-4 plus anti-PD-1 checkpoint blockade utilizes cellular mechanisms partially distinct from monotherapies. Proc Natl Acad Sci U S A *116*, 22699-22709. 10.1073/pnas.1821218116.

26. Chou, C., Zhang, X., Krishna, C., Nixon, B.G., Dadi, S., Capistrano, K.J., Kansler, E.R., Steele, M., Han, J., Shyu, A., et al. (2022). Programme of self-reactive innate-like T cell-mediated cancer immunity. Nature *605*, 139-145. 10.1038/s41586-022-04632-1.
27. Mitra, S., Malik, R., Wong, W., Rahman, A., Hartemink, A.J., Pritykin, Y., Dey, K.K., and Leslie, C.S. (2024). Single-cell multi-ome regression models identify functional and disease-associated enhancers and enable chromatin potential analysis. Nat Genet *56*, 627-636. 10.1038/s41588-024-01689-8.
28. DeTomaso, D., and Yosef, N. (2021). Hotspot identifies informative gene modules across modalities of single-cell genomics. Cell Syst *12*, 446-456 e449. 10.1016/j.cels.2021.04.005.
29. DeNardo, D.G., and Ruffell, B. (2019). Macrophages as regulators of tumour immunity and immunotherapy. Nat Rev Immunol *19*, 369-382. 10.1038/s41577-019-0127-6.
30. Schuette, V., Embgenbroich, M., Ulas, T., Welz, M., Schulte-Schrepping, J., Draffehn, A.M., Quast, T., Koch, K., Nehring, M., Konig, J., et al. (2016). Mannose receptor induces T-cell tolerance via inhibition of CD45 and up-regulation of CTLA-4. Proc Natl Acad Sci U S A *113*, 10649-10654. 10.1073/pnas.1605885113.
31. Rayes, R.F., Vourtzoumis, P., Bou Rjeily, M., Seth, R., Bourdeau, F., Giannias, B., Berube, J., Huang, Y.H., Rousseau, S., Camilleri-Broet, S., et al. (2020). Neutrophil Extracellular Trap-Associated CEACAM1 as a Putative Therapeutic Target to Prevent Metastatic Progression of Colon Carcinoma. J Immunol *204*, 2285-2294. 10.4049/jimmunol.1900240.
32. Zhao, J., Chen, X., Herjan, T., and Li, X. (2020). The role of interleukin-17 in tumor development and progression. J Exp Med *217*. 10.1084/jem.20190297.
33. Wang, K., Kim, M.K., Di Caro, G., Wong, J., Shalapour, S., Wan, J., Zhang, W., Zhong, Z., Sanchez-Lopez, E., Wu, L.W., et al. (2014). Interleukin-17 receptor a signaling in transformed enterocytes promotes early colorectal tumorigenesis. Immunity *41*, 1052-1063. 10.1016/j.immuni.2014.11.009.
34. Chung, L., Thiele Orberg, E., Geis, A.L., Chan, J.L., Fu, K., DeStefano Shields, C.E., Dejea, C.M., Fathi, P., Chen, J., Finard, B.B., et al. (2018). Bacteroides fragilis Toxin Coordinates a Pro-carcinogenic Inflammatory Cascade via Targeting of Colonic Epithelial Cells. Cell Host Microbe *23*, 203-214 e205. 10.1016/j.chom.2018.01.007.
35. Veglia, F., Perego, M., and Gabrilovich, D. (2018). Myeloid-derived suppressor cells coming of age. Nat Immunol *19*, 108-119. 10.1038/s41590-017-0022-x.
36. Goto, N., Westcott, P.M.K., Goto, S., Imada, S., Taylor, M.S., Eng, G., Braverman, J., Deshpande, V., Jacks, T., Agudo, J., and Yilmaz, O.H. (2024). SOX17 enables immune evasion of early colorectal adenomas and cancers. Nature *627*, 636-645. 10.1038/s41586-024-07135-3.
37. Huber, S., Gagliani, N., Esplugues, E., O'Connor, W., Jr., Huber, F.J., Chaudhry, A., Kamanaka, M., Kobayashi, Y., Booth, C.J., Rudensky, A.Y., et al. (2011). Th17 cells express interleukin-10 receptor and are controlled by Foxp3(-) and Foxp3+ regulatory CD4+ T cells in an interleukin-10-dependent manner. Immunity *34*, 554-565. 10.1016/j.immuni.2011.01.020.
38. Chaudhry, A., Samstein, R.M., Treuting, P., Liang, Y., Pils, M.C., Heinrich, J.M., Jack, R.S., Wunderlich, F.T., Bruning, J.C., Muller, W., and Rudensky, A.Y. (2011). Interleukin-10 signaling in regulatory T cells is required for suppression of Th17 cell-mediated inflammation. Immunity *34*, 566-578. 10.1016/j.immuni.2011.03.018.

39. Gu, Y., Yang, J., Ouyang, X., Liu, W., Li, H., Yang, J., Bromberg, J., Chen, S.H., Mayer, L., Unkeless, J.C., and Xiong, H. (2008). Interleukin 10 suppresses Th17 cytokines secreted by macrophages and T cells. Eur J Immunol *38*, 1807-1813. 10.1002/eji.200838331.
40. Oliveira, M.F., Romero, J.P., Chung, M., Williams, S., Gottscho, A.D., Gupta, A., Pilipauskas, S.E., Mohabbat, S., Raman, N., Sukovich, D., et al. (2024). Characterization of immune cell populations in the tumor microenvironment of colorectal cancer using high definition spatial profiling. Biorxiv. 10.1101/2024.06.04.597233.
41. Chu, Y., Dai, E., Li, Y., Han, G., Pei, G., Ingram, D.R., Thakkar, K., Qin, J.J., Dang, M., Le, X., et al. (2023). Pan-cancer T cell atlas links a cellular stress response state to immunotherapy resistance. Nat Med *29*, 1550-1562. 10.1038/s41591-023-02371-y.
42. Ramanan, D., Pratama, A., Zhu, Y., Venezia, O., Sassone-Corsi, M., Chowdhary, K., Galvan-Pena, S., Sefik, E., Brown, C., Gelineau, A., et al. (2023). Regulatory T cells in the face of the intestinal microbiota. Nat Rev Immunol *23*, 749-762. 10.1038/s41577-023-00890-w.
43. Gasteiger, G., Hemmers, S., Firth, M.A., Le Floc'h, A., Huse, M., Sun, J.C., and Rudensky, A.Y. (2013). IL-2-dependent tuning of NK cell sensitivity for target cells is controlled by regulatory T cells. J Exp Med *210*, 1167-1178. 10.1084/jem.20122462.
44. Sawant, D.V., Yano, H., Chikina, M., Zhang, Q., Liao, M., Liu, C., Callahan, D.J., Sun, Z., Sun, T., Tabib, T., et al. (2019). Adaptive plasticity of IL-10(+) and IL-35(+) T(reg) cells cooperatively promotes tumor T cell exhaustion. Nat Immunol *20*, 724-735. 10.1038/s41590-019-0346-9.
45. Green, J.A., Arpaia, N., Schizas, M., Dobrin, A., and Rudensky, A.Y. (2017). A nonimmune function of T cells in promoting lung tumor progression. J Exp Med *214*, 3565-3575. 10.1084/jem.20170356.
46. Kamada, T., Togashi, Y., Tay, C., Ha, D., Sasaki, A., Nakamura, Y., Sato, E., Fukuoka, S., Tada, Y., Tanaka, A., et al. (2019). PD-1(+) regulatory T cells amplified by PD-1 blockade promote hyperprogression of cancer. Proc Natl Acad Sci U S A *116*, 9999-10008. 10.1073/pnas.1822001116.
47. Levine, A.G., Arvey, A., Jin, W., and Rudensky, A.Y. (2014). Continuous requirement for the TCR in regulatory T cell function. Nat Immunol *15*, 1070-1078. 10.1038/ni.3004.
48. Vahl, J.C., Drees, C., Heger, K., Heink, S., Fischer, J.C., Nedjic, J., Ohkura, N., Morikawa, H., Poeck, H., Schallenberg, S., et al. (2014). Continuous T cell receptor signals maintain a functional regulatory T cell pool. Immunity *41*, 722-736. 10.1016/j.immuni.2014.10.012.
49. Chinen, T., Kannan, A.K., Levine, A.G., Fan, X., Klein, U., Zheng, Y., Gasteiger, G., Feng, Y., Fontenot, J.D., and Rudensky, A.Y. (2016). An essential role for the IL-2 receptor in T(reg) cell function. Nat Immunol *17*, 1322-1333. 10.1038/ni.3540.
50. Martins, G.A., Cimmino, L., Liao, J., Magnusdottir, E., and Calame, K. (2008). Blimp-1 directly represses Il2 and the Il2 activator Fos, attenuating T cell proliferation and survival. J Exp Med *205*, 1959-1965. 10.1084/jem.20080526.
51. Neumann, C., Blume, J., Roy, U., Teh, P.P., Vasanthakumar, A., Beller, A., Liao, Y., Heinrich, F., Arenzana, T.L., Hackney, J.A., et al. (2019). c-Maf-dependent T(reg) cell control of intestinal T(H)17 cells and IgA establishes host-microbiota homeostasis. Nat Immunol *20*, 471-481. 10.1038/s41590-019-0316-2.

52. Ogawa, C., Bankoti, R., Nguyen, T., Hassanzadeh-Kiabi, N., Nadeau, S., Porritt, R.A., Couse, M., Fan, X., Dhall, D., Eberl, G., et al. (2018). Blimp-1 Functions as a Molecular Switch to Prevent Inflammatory Activity in Foxp3(+)RORgammat(+) Regulatory T Cells. Cell Rep *25*, 19-28 e15. 10.1016/j.celrep.2018.09.016.
53. Cretney, E., Leung, P.S., Trezise, S., Newman, D.M., Rankin, L.C., Teh, C.E., Putoczki, T.L., Gray, D.H., Belz, G.T., Mielke, L.A., et al. (2018). Characterization of Blimp-1 function in effector regulatory T cells. J Autoimmun *91*, 73-82. 10.1016/j.jaut.2018.04.003.
54. Majumder, S., and McGeachy, M.J. (2021). IL-17 in the Pathogenesis of Disease: Good Intentions Gone Awry. Annu Rev Immunol *39*, 537-556. 10.1146/annurev-immunol-101819-092536.
55. Perez, L.G., Kempski, J., McGee, H.M., Pelzcar, P., Agalioti, T., Giannou, A., Konczalla, L., Brockmann, L., Wahib, R., Xu, H., et al. (2020). TGF-beta signaling in Th17 cells promotes IL-22 production and colitis-associated colon cancer. Nat Commun *11*, 2608. 10.1038/s41467-020-16363-w.
56. De Simone, M., Arrigoni, A., Rossetti, G., Gruarin, P., Ranzani, V., Politano, C., Bonnal, R.J.P., Provasi, E., Sarnicola, M.L., Panzeri, I., et al. (2016). Transcriptional Landscape of Human Tissue Lymphocytes Unveils Uniqueness of Tumor-Infiltrating T Regulatory Cells. Immunity *45*, 1135-1147. 10.1016/j.immuni.2016.10.021.
57. Villarreal, D.O., L'Huillier, A., Armington, S., Mottershead, C., Filippova, E.V., Coder, B.D., Petit, R.G., and Princiotta, M.F. (2018). Targeting CCR8 Induces Protective Antitumor Immunity and Enhances Vaccine-Induced Responses in Colon Cancer. Cancer Res *78*, 5340-5348. 10.1158/0008-5472.CAN-18-1119.
58. Campbell, J.R., McDonald, B.R., Mesko, P.B., Siemers, N.O., Singh, P.B., Selby, M., Sproul, T.W., Korman, A.J., Vlach, L.M., Houser, J., et al. (2021). Fc-Optimized Anti-CCR8 Antibody Depletes Regulatory T Cells in Human Tumor Models. Cancer Res *81*, 2983-2994. 10.1158/0008-5472.CAN-20-3585.
59. Glasner, A., Rose, S.A., Sharma, R., Gudjonson, H., Chu, T., Green, J.A., Rampersaud, S., Valdez, I.K., Andretta, E.S., Dhillon, B.S., et al. (2023). Conserved transcriptional connectivity of regulatory T cells in the tumor microenvironment informs new combination cancer therapy strategies. Nat Immunol *24*, 1020-1035. 10.1038/s41590-023-01504-2.
60. Levine, A.G., Mendoza, A., Hemmers, S., Moltedo, B., Niec, R.E., Schizas, M., Hoyos, B.E., Putintseva, E.V., Chaudhry, A., Dikiy, S., et al. (2017). Stability and function of regulatory T cells expressing the transcription factor T-bet. Nature *546*, 421-425. 10.1038/nature22360.
61. Kim, J.M., Rasmussen, J.P., and Rudensky, A.Y. (2007). Regulatory T cells prevent catastrophic autoimmunity throughout the lifespan of mice. Nat Immunol *8*, 191-197. 10.1038/ni1428.
62. Fujii, M., Matano, M., Nanki, K., and Sato, T. (2015). Efficient genetic engineering of human intestinal organoids using electroporation. Nat Protoc *10*, 1474-1485. 10.1038/nprot.2015.088.
63. Granja, J.M., Corces, M.R., Pierce, S.E., Bagdatli, S.T., Choudhry, H., Chang, H.Y., and Greenleaf, W.J. (2021). ArchR is a scalable software package for integrative single-cell chromatin accessibility analysis. Nat Genet *53*, 403-411. 10.1038/s41588-021-00790-6.

64. Johnson, W.E., Li, C., and Rabinovic, A. (2007). Adjusting batch effects in microarray expression data using empirical Bayes methods. Biostatistics *8*, 118-127. 10.1093/biostatistics/kxj037.
65. Wolf, F.A., Angerer, P., and Theis, F.J. (2018). SCANPY: large-scale single-cell gene expression data analysis. Genome Biol *19*, 15. 10.1186/s13059-017-1382-0.
66. Tayyebi, Z., Pine, A.R., and Leslie, C.S. (2024). Scalable and unbiased sequence-informed embedding of single-cell ATAC-seq data with CellSpace. Nat Methods *21*, 1014-1022. 10.1038/s41592-024-02274-x.
67. Feng, J., Liu, T., Qin, B., Zhang, Y., and Liu, X.S. (2012). Identifying ChIP-seq enrichment using MACS. Nat Protoc *7*, 1728-1740. 10.1038/nprot.2012.101.
68. Schep, A.N., Wu, B., Buenrostro, J.D., and Greenleaf, W.J. (2017). chromVAR: inferring transcription-factor-associated accessibility from single-cell epigenomic data. Nat Methods *14*, 975-978. 10.1038/nmeth.4401.
69. Mages, S., Moriel, N., Avraham-Davidi, I., Murray, E., Watter, J., Chen, F., Rozenblatt-Rosen, O., Klughammer, J., Regev, A., and Nitzan, M. (2023). TACCO unifies annotation transfer and decomposition of cell identities for single-cell and spatial omics. Nat Biotechnol *41*, 1465-1473. 10.1038/s41587-023-01657-3.
70. Chu, T., Wang, Z., Pe'er, D., and Danko, C.G. (2022). Cell type and gene expression deconvolution with BayesPrism enables Bayesian integrative analysis across bulk and single-cell RNA sequencing in oncology. Nat Cancer *3*, 505-517. 10.1038/s43018-022-00356-3.

Figure 1

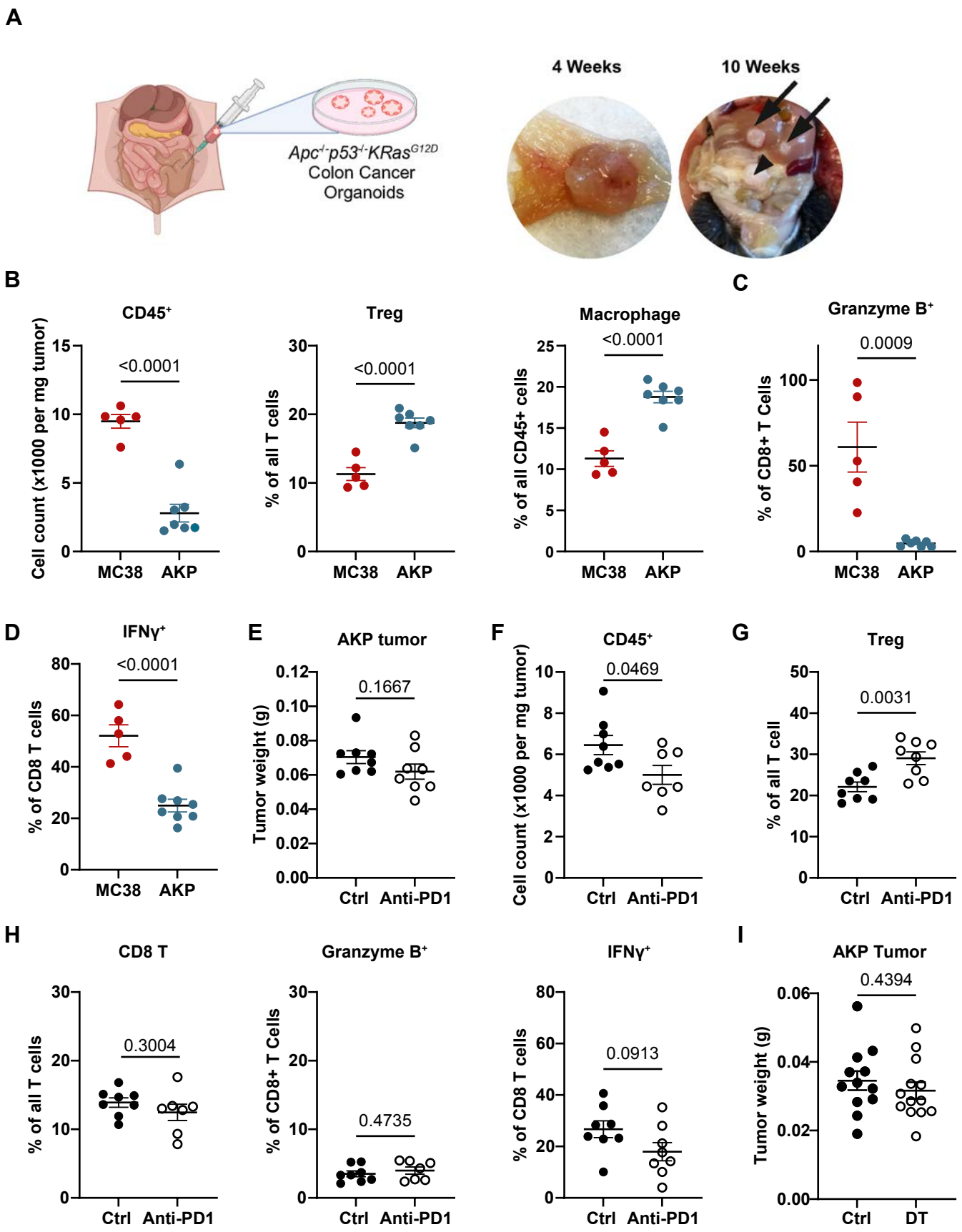
A
Apc-/-p53-/-KRasG12D
Colon Cancer
Organoids
4 Weeks
10 Weeks
B
CD45+
Cell count (x1000 per mg tumor)
<0.0001
MC38
AKP
Treg
% of all T cells
<0.0001
Macrophage
% of all CD45+ cells
<0.0001
C
Granzyme B+
% of CD8+ T Cells
0.0009
D
IFNγ+
% of CD8 T cells
<0.0001
E
AKP tumor
Tumor weight (g)
0.1667
Ctrl
Anti-PD1
F
CD45+
Cell count (x1000 per mg tumor)
0.0469
G
Treg
% of all T cell
0.0031
H
CD8 T
% of all T cells
0.3004
Granzyme B+
% of CD8+ T Cells
0.4735
IFNγ+
% of CD8 T cells
0.0913
I
AKP Tumor
Tumor weight (g)
0.4394
DT

Figure 2

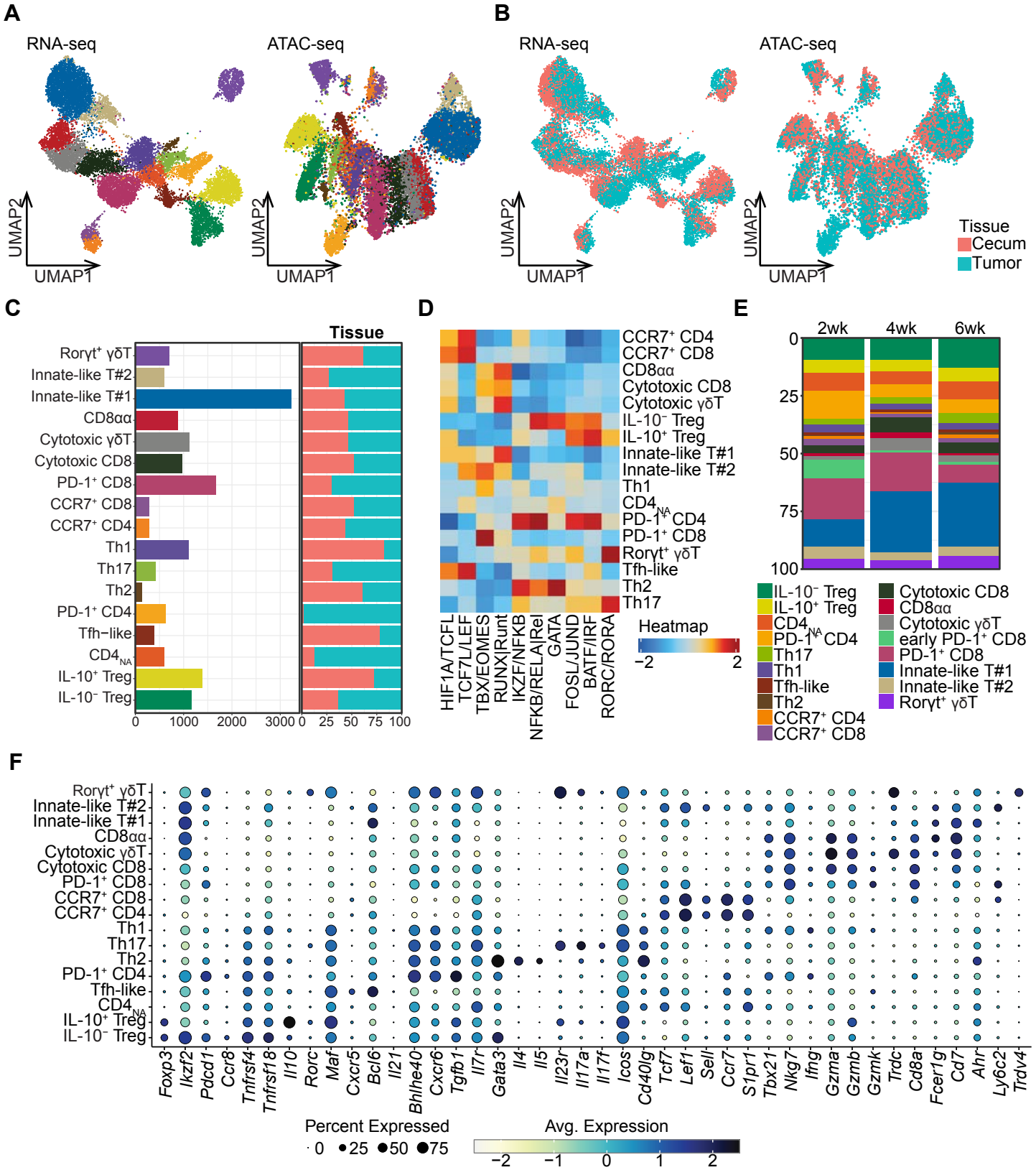
A
RNA-seq
ATAC-seq
UMAP2
UMAP1
B
RNA-seq
ATAC-seq
Tissue
Cecum
Tumor
C
Tissue
Rorγt⁺ γδT
Innate-like T#2
Innate-like T#1
CD8αα
Cytotoxic γδT
Cytotoxic CD8
PD-1⁺ CD8
CCR7⁺ CD8
CCR7⁺ CD4
Th1
Th17
Th2
PD-1⁺ CD4
Tfh−like
CD4NA
IL-10⁺ Treg
IL-10⁻ Treg
0 1000 2000 3000
0 25 50 75 100
D
CCR7⁺ CD4
CCR7⁺ CD8
CD8αα
Cytotoxic CD8
Cytotoxic γδT
IL-10⁻ Treg
IL-10⁺ Treg
Innate-like T#1
Innate-like T#2
Th1
CD4NA
PD-1⁺ CD4
PD-1⁺ CD8
Rorγt⁺ γδT
Tfh-like
Th2
Th17
HIF1A/TCFL
TCF7L/LEF
TBX/EOMES
RUNX|Runt
IKZF/NFKB
NFKB/RELA|Rel
GATA
FOSL/JUND
BATF/IRF
RORC/RORA
Heatmap
−2
2
E
2wk
4wk
6wk
0
25
50
75
100
IL-10⁻ Treg
IL-10⁺ Treg
CD4NA
PD-1⁺ CD4
Th17
Th1
Tfh-like
Th2
CCR7⁺ CD4
CCR7⁺ CD8
Cytotoxic CD8
CD8αα
Cytotoxic γδT
early PD-1⁺ CD8
PD-1⁺ CD8
Innate-like T#1
Innate-like T#2
Rorγt⁺ γδT
F
Rorγt⁺ γδT
Innate-like T#2
Innate-like T#1
CD8αα
Cytotoxic γδT
Cytotoxic CD8
PD-1⁺ CD8
CCR7⁺ CD8
CCR7⁺ CD4
Th1
Th17
Th2
PD-1⁺ CD4
Tfh-like
CD4NA
IL-10⁺ Treg
IL-10⁻ Treg
Foxp3
Ikzf2
Pdcd1
Ccr8
Tnfrsf4
Tnfrsf18
Il10
Rorc
Maf
Cxcr5
Bcl6
Il21
Bhlhe40
Cxcr6
Tgfb1
Il7r
Gata3
Il4
Il5
Il23r
Il17a
Il17f
Icos
Cd40lg
Tcf7
Lef1
Sell
Ccr7
S1pr1
Tbx21
Nkg7
Ifng
Gzma
Gzmb
Gzmk
Trdc
Cd8a
Fcer1g
Cd7
Ahr
Ly6c2
Trdv4
Percent Expressed
0 25 50 75
Avg. Expression
−2 −1 0 1 2

Figure 3

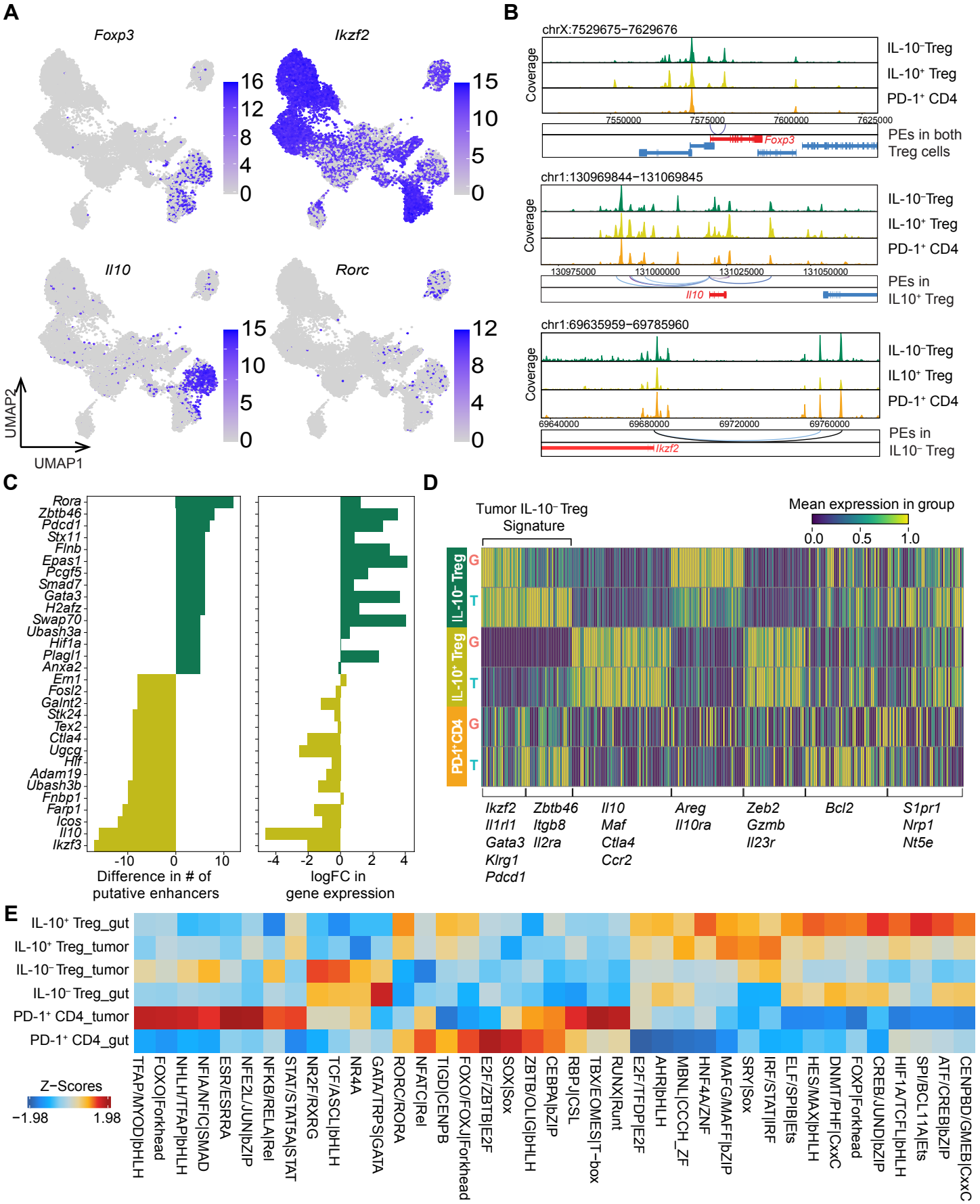
A
Foxp3
Ikzf2
Il10
Rorc
UMAP2
UMAP1
B
chrX:7529675−7629676
Coverage
IL-10⁻Treg
IL-10⁺ Treg
PD-1⁺ CD4
PEs in both Treg cells
Foxp3
chr1:130969844−131069845
PEs in IL10⁺ Treg
Il10
chr1:69635959−69785960
PEs in IL10⁻ Treg
Ikzf2
C
Rora
Zbtb46
Pdcd1
Stx11
Flnb
Epas1
Pcgf5
Smad7
Gata3
H2afz
Swap70
Ubash3a
Hif1a
Plagl1
Anxa2
Ern1
Fosl2
Galnt2
Stk24
Tex2
Ctla4
Ugcg
Hif
Adam19
Ubash3b
Fnbp1
Farp1
Icos
Il10
Ikzf3
Difference in # of putative enhancers
logFC in gene expression
D
Tumor IL-10⁻ Treg Signature
Mean expression in group
IL-10⁻ Treg
IL-10⁺ Treg
PD-1⁺CD4
G
T
Ikzf2 Il1rl1 Gata3 Klrg1 Pdcd1
Zbtb46 Itgb8 Il2ra
Il10 Maf Ctla4 Ccr2
Areg Il10ra
Zeb2 Gzmb Il23r
Bcl2
S1pr1 Nrp1 Nt5e
E
IL-10⁺ Treg_gut
IL-10⁺ Treg_tumor
IL-10⁻ Treg_tumor
IL-10⁻ Treg_gut
PD-1⁺ CD4_tumor
PD-1⁺ CD4_gut
Z−Scores
−1.98
1.98
TFAP/MYOD|bHLH
FOXO|Forkhead
NHLH/TFAP|bHLH
NFIA/NFIC|SMAD
ESR/ESRRA
NFE2L/JUN|bZIP
NFKB/RELA|Rel
STAT/STAT5A|STAT
NR2F/RXRG
TCF/ASCL|bHLH
NR4A
GATA/TRPS|GATA
RORC/RORA
NFATC|Rel
TIGD|CENPB
FOXO/FOXJ|Forkhead
E2F/ZBTB|E2F
SOX|Sox
ZBTB/OLIG|bHLH
CEBPA|bZIP
RBPJ|CSL
TBX/EOMES|T−box
RUNX|Runt
E2F/TFDP|E2F
AHR|bHLH
MBNL|CCCH_ZF
HNF4A/ZNF
MAFG/MAFF|bZIP
SRY|Sox
IRF/STAT|IRF
ELF/SPI|Ets
HES/MAX|bHLH
DNMT/PHF|CxxC
FOXP|Forkhead
CREB/JUND|bZIP
HIF1A/TCFL|bHLH
SPI/BCL11A|Ets
ATF/CREB|bZIP
CENPBD/GMEB|CxxC

Figure 4

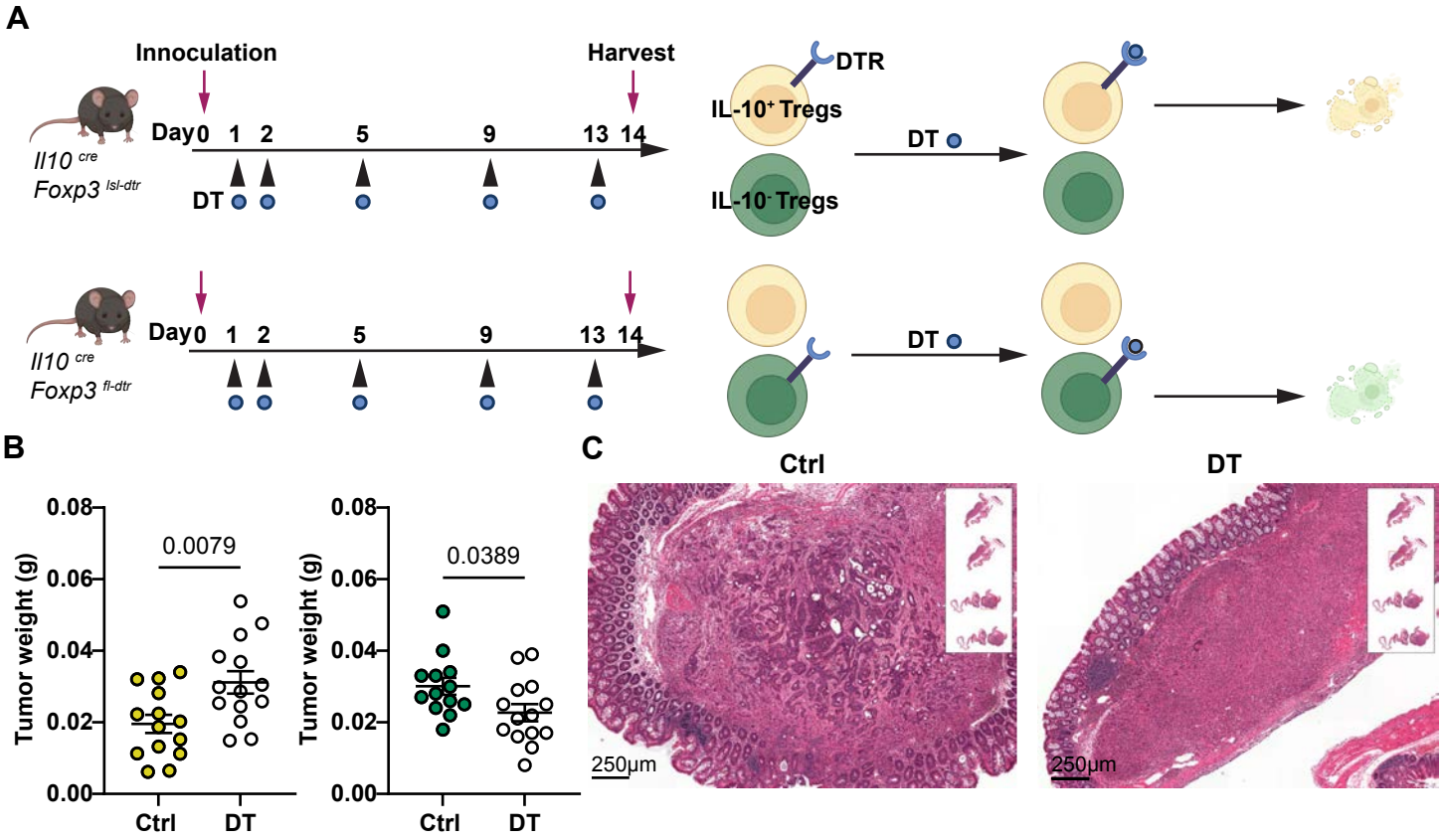
A
Innoculation
Harvest
Day 0 1 2 5 9 13 14
DT
Il10 cre
Foxp3 lsl-dtr
DTR
IL-10+ Tregs
IL-10- Tregs
DT
Il10 cre
Foxp3 fl-dtr
B
Tumor weight (g)
0.08
0.06
0.04
0.02
0.00
0.0079
0.0389
Ctrl
DT
C
Ctrl
DT
250μm
250μm

Figure 5

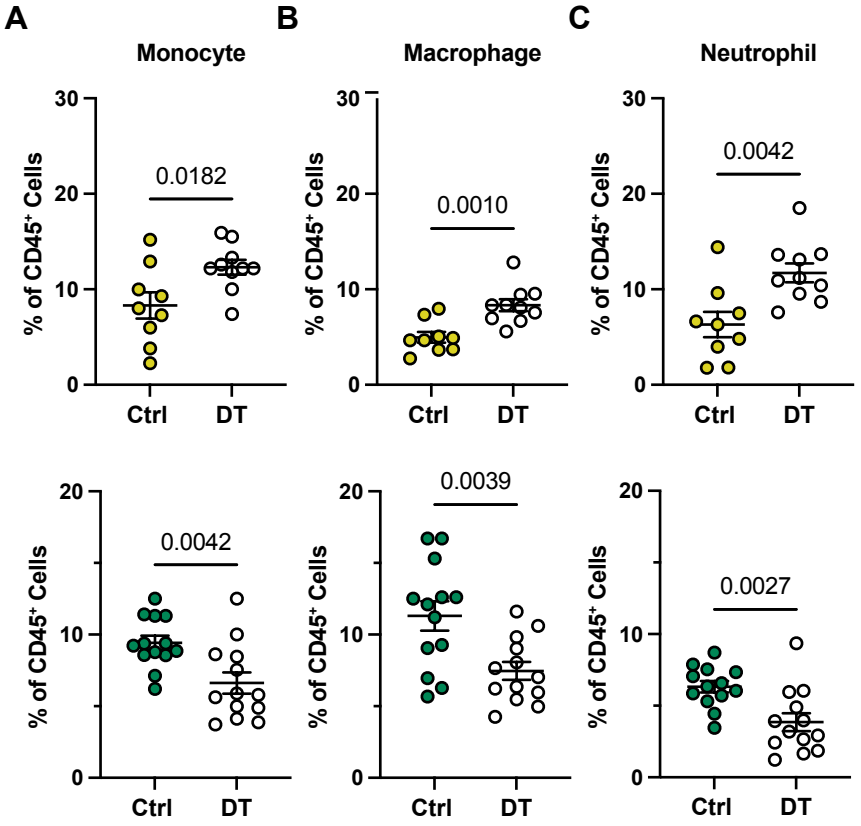
A
B
C
Monocyte
Macrophage
Neutrophil
% of CD45+ Cells
0.0182
0.0010
0.0042
0.0042
0.0039
0.0027
Ctrl
DT

Figure 6

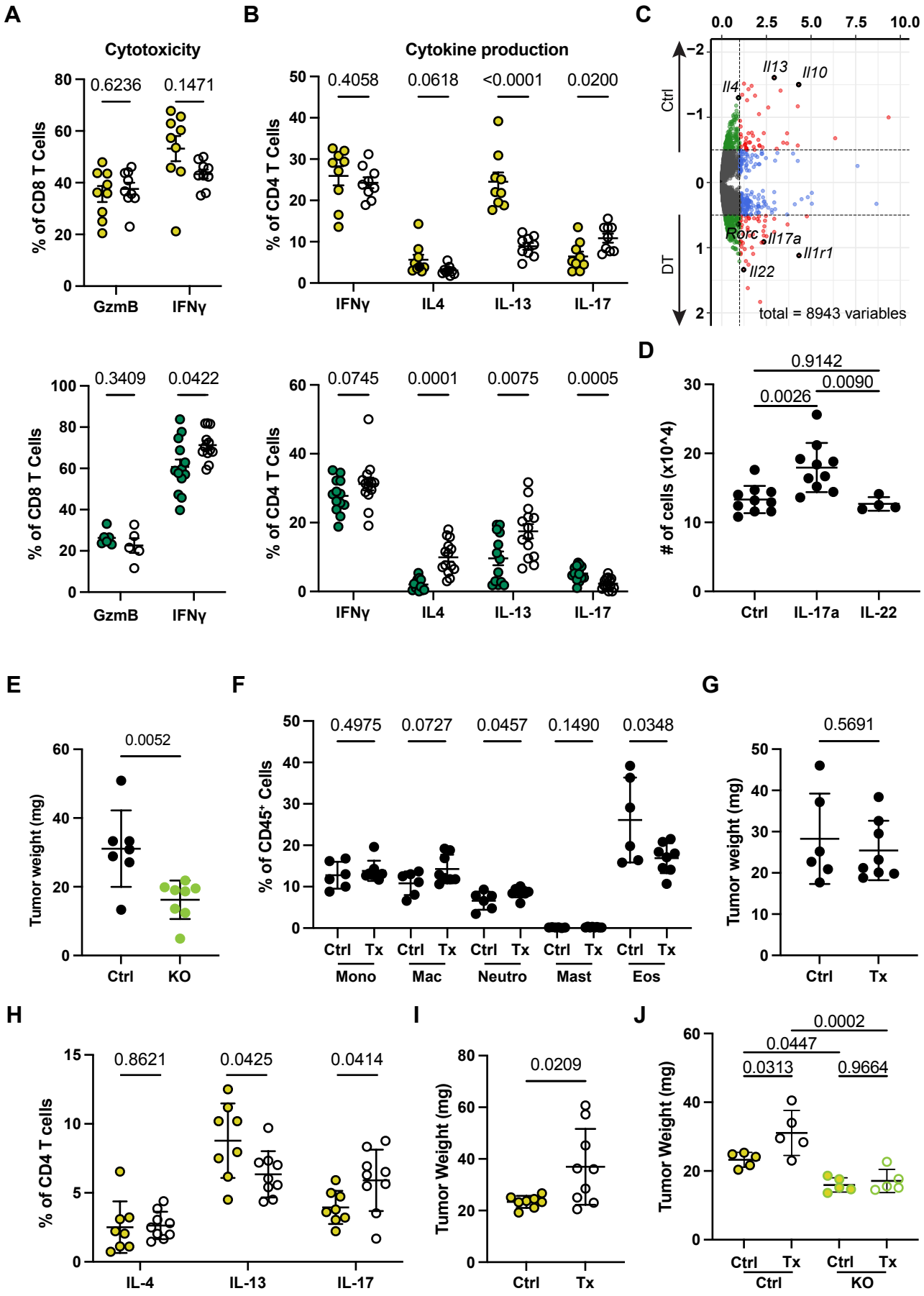
A
Cytotoxicity
% of CD8 T Cells
0.6236
0.1471
GzmB
IFNγ
0.3409
0.0422
B
Cytokine production
% of CD4 T Cells
0.4058
0.0618
<0.0001
0.0200
IFNγ
IL4
IL-13
IL-17
0.0745
0.0001
0.0075
0.0005
C
Ctrl
DT
Il13
Il10
Il4
Rorc
Il17a
Il1r1
Il22
total = 8943 variables
D
# of cells (x10^4)
0.9142
0.0090
0.0026
Ctrl
IL-17a
IL-22
E
Tumor weight (mg)
0.0052
Ctrl
KO
F
% of CD45+ Cells
0.4975
0.0727
0.0457
0.1490
0.0348
Ctrl
Tx
Mono
Mac
Neutro
Mast
Eos
G
Tumor weight (mg)
0.5691
Ctrl
Tx
H
% of CD4 T cells
0.8621
0.0425
0.0414
IL-4
IL-13
IL-17
I
Tumor Weight (mg)
0.0209
Ctrl
Tx
J
Tumor Weight (mg)
0.0002
0.0447
0.0313
0.9664
Ctrl
Tx
Ctrl
KO

Figure 7

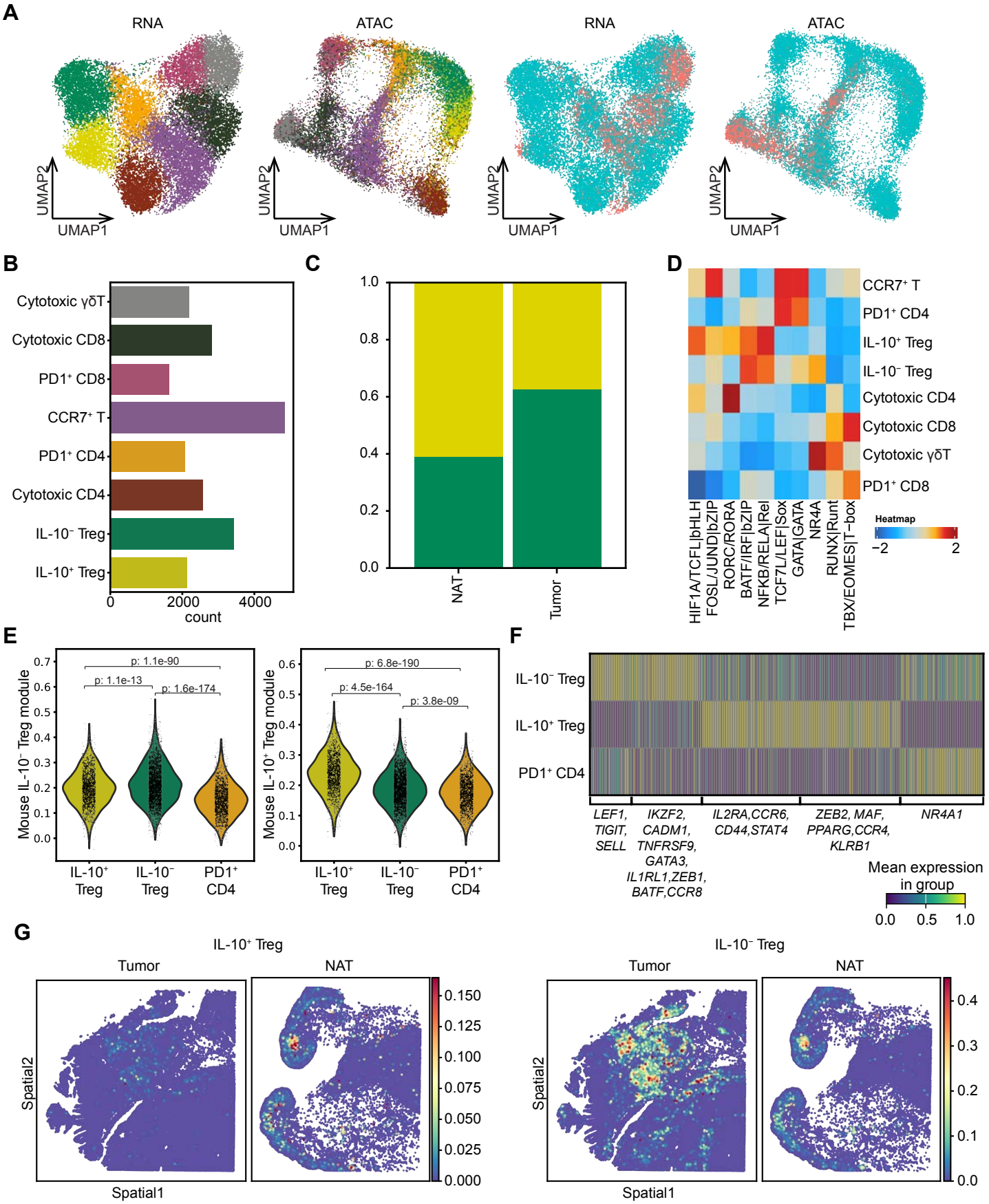
A
RNA
ATAC
RNA
ATAC
UMAP2
UMAP1
B
Cytotoxic γδT
Cytotoxic CD8
PD1⁺ CD8
CCR7⁺ T
PD1⁺ CD4
Cytotoxic CD4
IL-10⁻ Treg
IL-10⁺ Treg
0
2000
4000
count
C
1.0
0.8
0.6
0.4
0.2
0.0
NAT
Tumor
D
CCR7⁺ T
PD1⁺ CD4
IL-10⁺ Treg
IL-10⁻ Treg
Cytotoxic CD4
Cytotoxic CD8
Cytotoxic γδT
PD1⁺ CD8
HIF1A/TCFL|bHLH
FOSL/JUND|bZIP
RORC/RORA
BATF/IRF|bZIP
NFKB/RELA|Rel
TCF7L/LEF|Sox
GATA|GATA
NR4A
RUNX|Runt
TBX/EOMES|T−box
Heatmap
−2
2
E
Mouse IL-10⁻ Treg module
p: 1.1e-90
p: 1.1e-13
p: 1.6e-174
IL-10⁺ Treg
IL-10⁻ Treg
PD1⁺ CD4
Mouse IL-10⁺ Treg module
p: 6.8e-190
p: 4.5e-164
p: 3.8e-09
IL-10⁺ Treg
IL-10⁻ Treg
PD1⁺ CD4
F
IL-10⁻ Treg
IL-10⁺ Treg
PD1⁺ CD4
LEF1, TIGIT, SELL
IKZF2, CADM1, TNFRSF9, GATA3, IL1RL1,ZEB1, BATF,CCR8
IL2RA,CCR6, CD44,STAT4
ZEB2, MAF, PPARG,CCR4, KLRB1
NR4A1
Mean expression in group
0.0
0.5
1.0
G
IL-10⁺ Treg
Tumor
NAT
Spatial2
Spatial1
0.150
0.125
0.100
0.075
0.050
0.025
0.000
IL-10⁻ Treg
Tumor
NAT
Spatial2
Spatial1
0.4
0.3
0.2
0.1
0.0

Figure S1

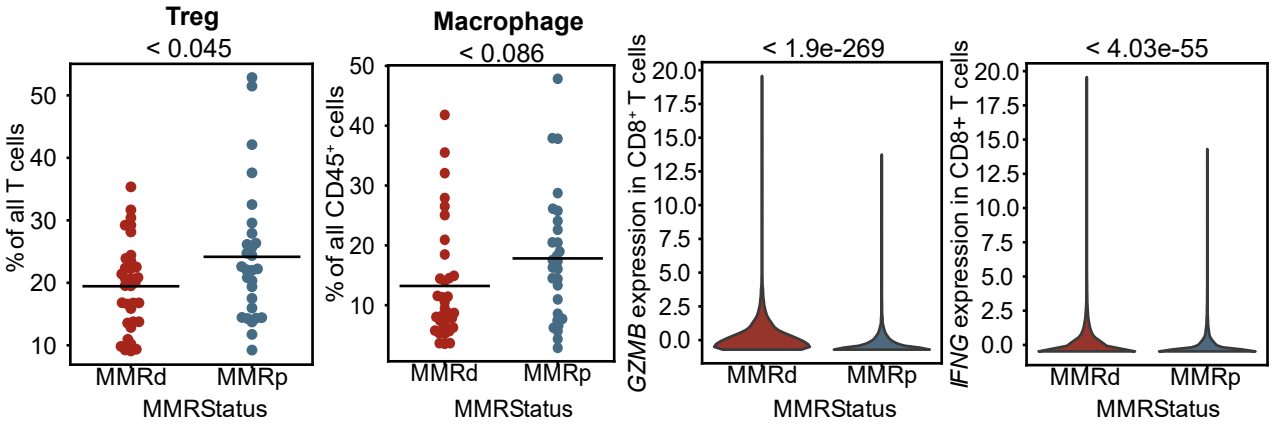
Treg
< 0.045
% of all T cells
50
40
30
20
10
MMRd
MMRp
MMRStatus
Macrophage
< 0.086
% of all CD45⁺ cells
50
40
30
20
10
MMRd
MMRp
MMRStatus
< 1.9e-269
GZMB expression in CD8⁺ T cells
20.0
17.5
15.0
12.5
10.0
7.5
5.0
2.5
0.0
MMRd
MMRp
MMRStatus
< 4.03e-55
IFNG expression in CD8+ T cells
20.0
17.5
15.0
12.5
10.0
7.5
5.0
2.5
0.0
MMRd
MMRp
MMRStatus

Figure S2

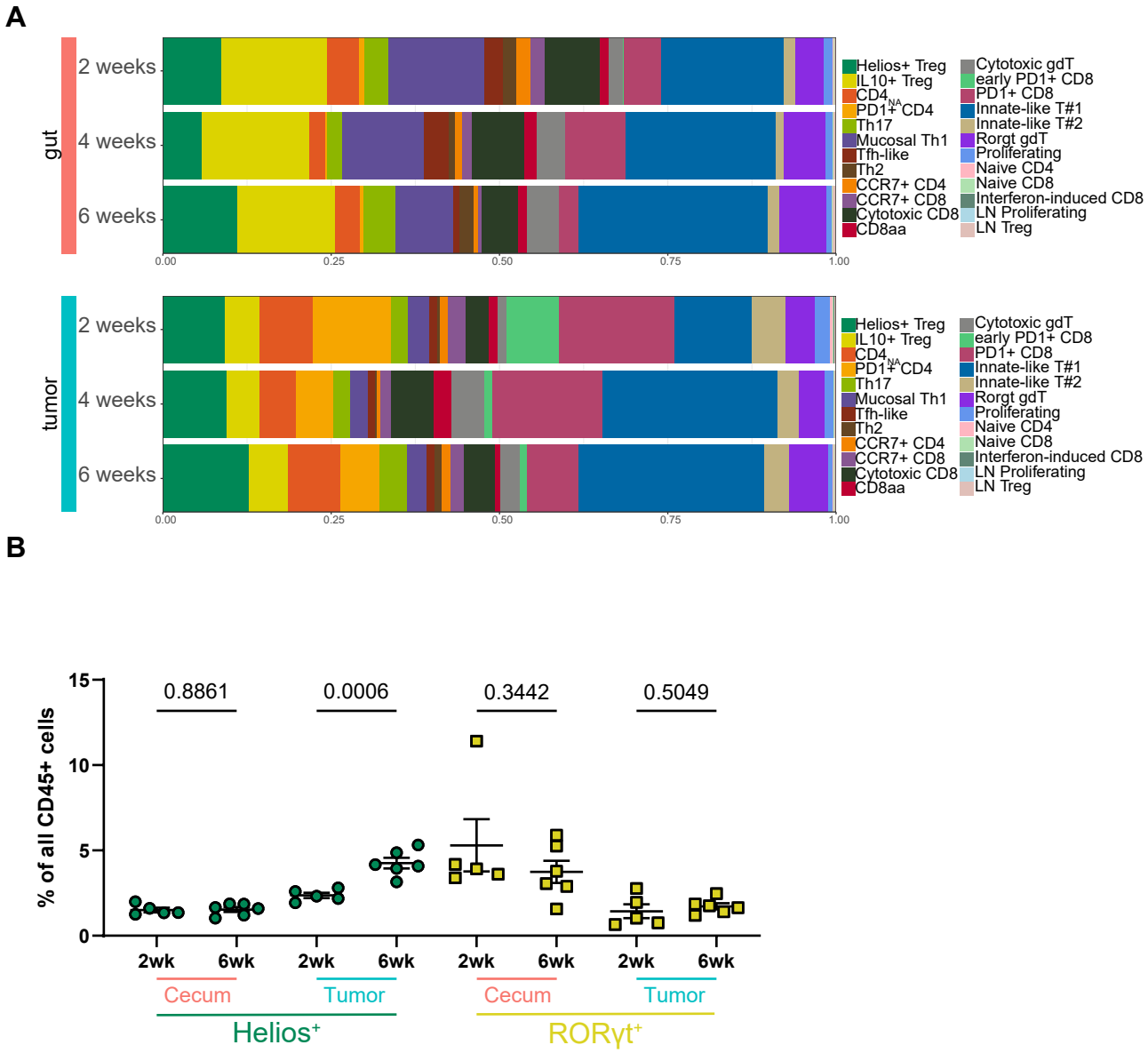
A
gut
2 weeks
4 weeks
6 weeks
tumor
2 weeks
4 weeks
6 weeks
0.00
0.25
0.50
0.75
1.00
Helios+ Treg
IL10+ Treg
CD4NA
PD1+ CD4
Th17
Mucosal Th1
Tfh-like
Th2
CCR7+ CD4
CCR7+ CD8
Cytotoxic CD8
CD8aa
Cytotoxic gdT
early PD1+ CD8
PD1+ CD8
Innate-like T#1
Innate-like T#2
Rorgt gdT
Proliferating
Naive CD4
Naive CD8
Interferon-induced CD8
LN Proliferating
LN Treg
B
% of all CD45+ cells
15
10
5
0
0.8861
0.0006
0.3442
0.5049
2wk
6wk
2wk
6wk
2wk
6wk
2wk
6wk
Cecum
Tumor
Cecum
Tumor
Helios+
RORγt+

Figure S3

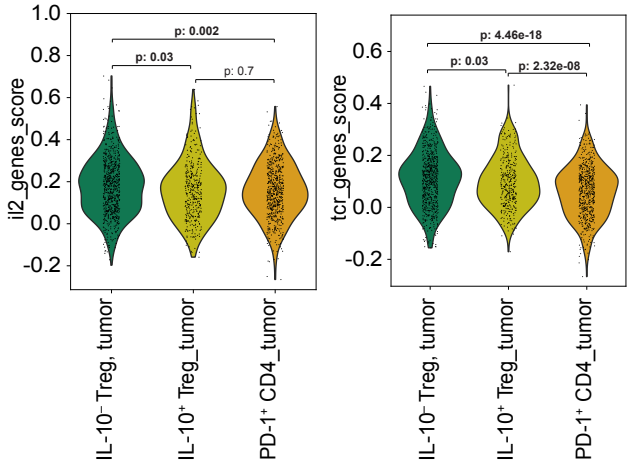
il2_genes_score
1.0
0.8
0.6
0.4
0.2
0.0
-0.2
p: 0.002
p: 0.03
p: 0.7
IL-10⁻ Treg, tumor
IL-10⁺ Treg_tumor
PD-1⁺ CD4_tumor
tcr_genes_score
0.6
0.4
0.2
0.0
-0.2
p: 4.46e-18
p: 0.03
p: 2.32e-08
IL-10⁻ Treg, tumor
IL-10⁺ Treg_tumor
PD-1⁺ CD4_tumor

Figure S4

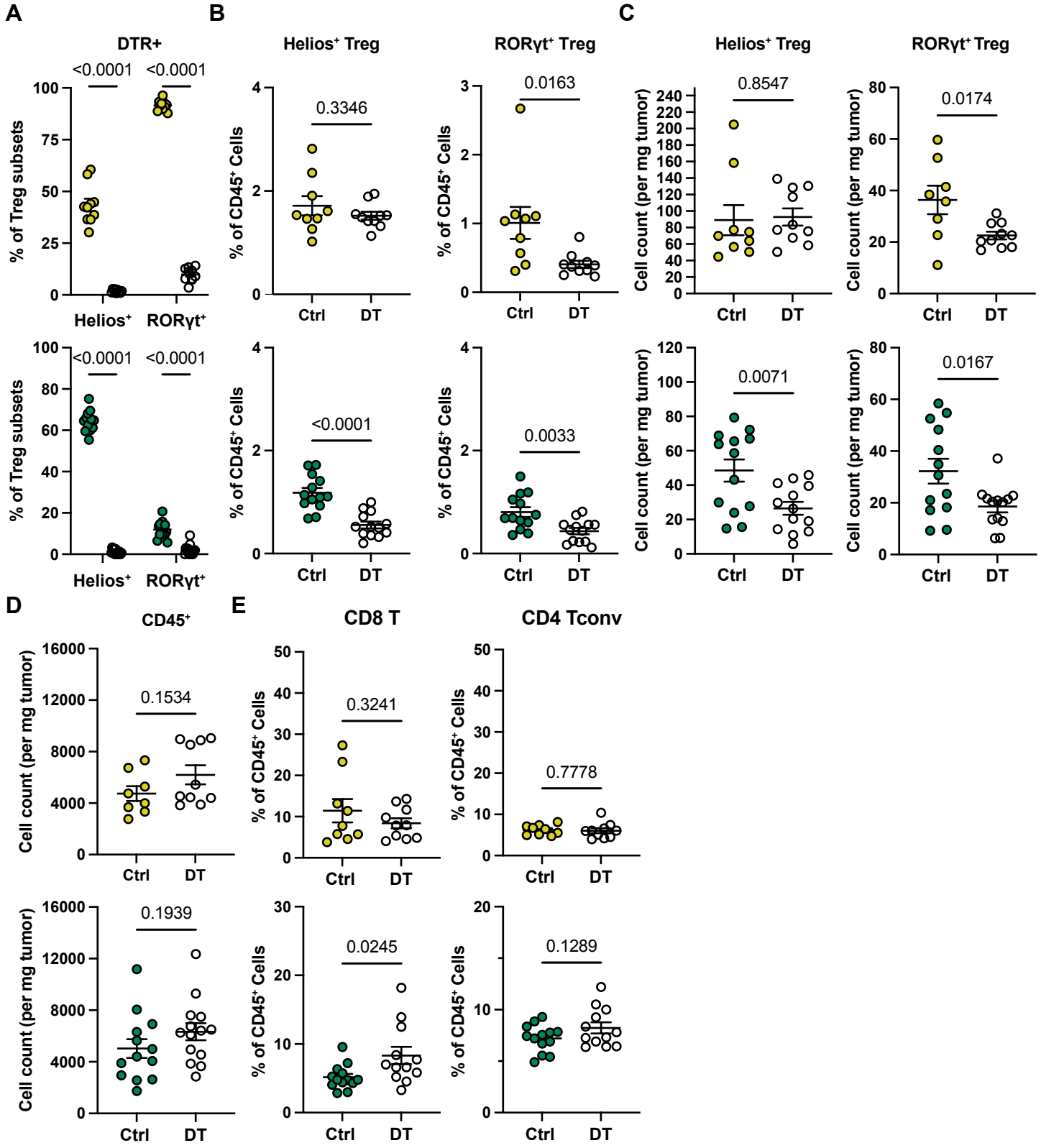
A
B
C
DTR+
Helios⁺ Treg
RORγt⁺ Treg
Helios⁺ Treg
RORγt⁺ Treg
% of Treg subsets
% of CD45⁺ Cells
Cell count (per mg tumor)
<0.0001
<0.0001
0.3346
0.0163
0.8547
0.0174
<0.0001
0.0033
0.0071
0.0167
Helios⁺
RORγt⁺
Ctrl
DT
D
E
CD45⁺
CD8 T
CD4 Tconv
0.1534
0.3241
0.7778
0.1939
0.0245
0.1289

Figure S5

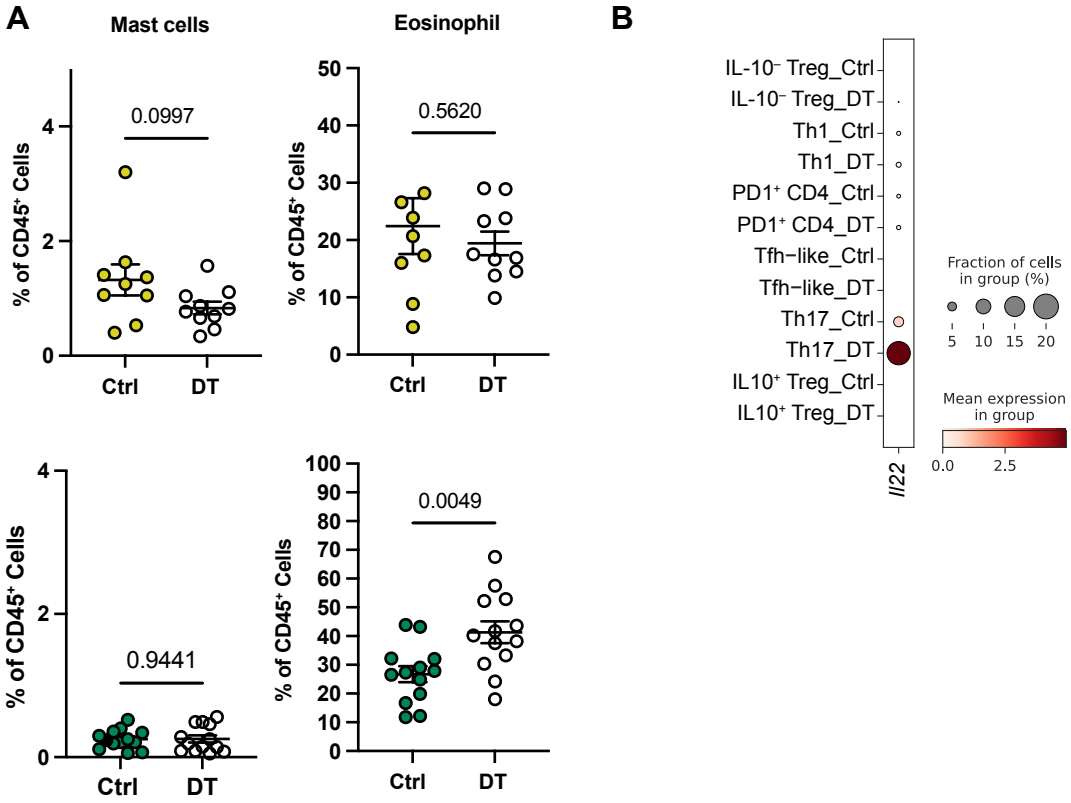
A
Mast cells
Eosinophil
0.0997
0.5620
0.9441
0.0049
% of CD45⁺ Cells
Ctrl
DT
B
IL-10⁻ Treg_Ctrl
IL-10⁻ Treg_DT
Th1_Ctrl
Th1_DT
PD1⁺ CD4_Ctrl
PD1⁺ CD4_DT
Tfh−like_Ctrl
Tfh−like_DT
Th17_Ctrl
Th17_DT
IL10⁺ Treg_Ctrl
IL10⁺ Treg_DT
Il22
Fraction of cells in group (%)
5 10 15 20
Mean expression in group
0.0 2.5

Figure S6

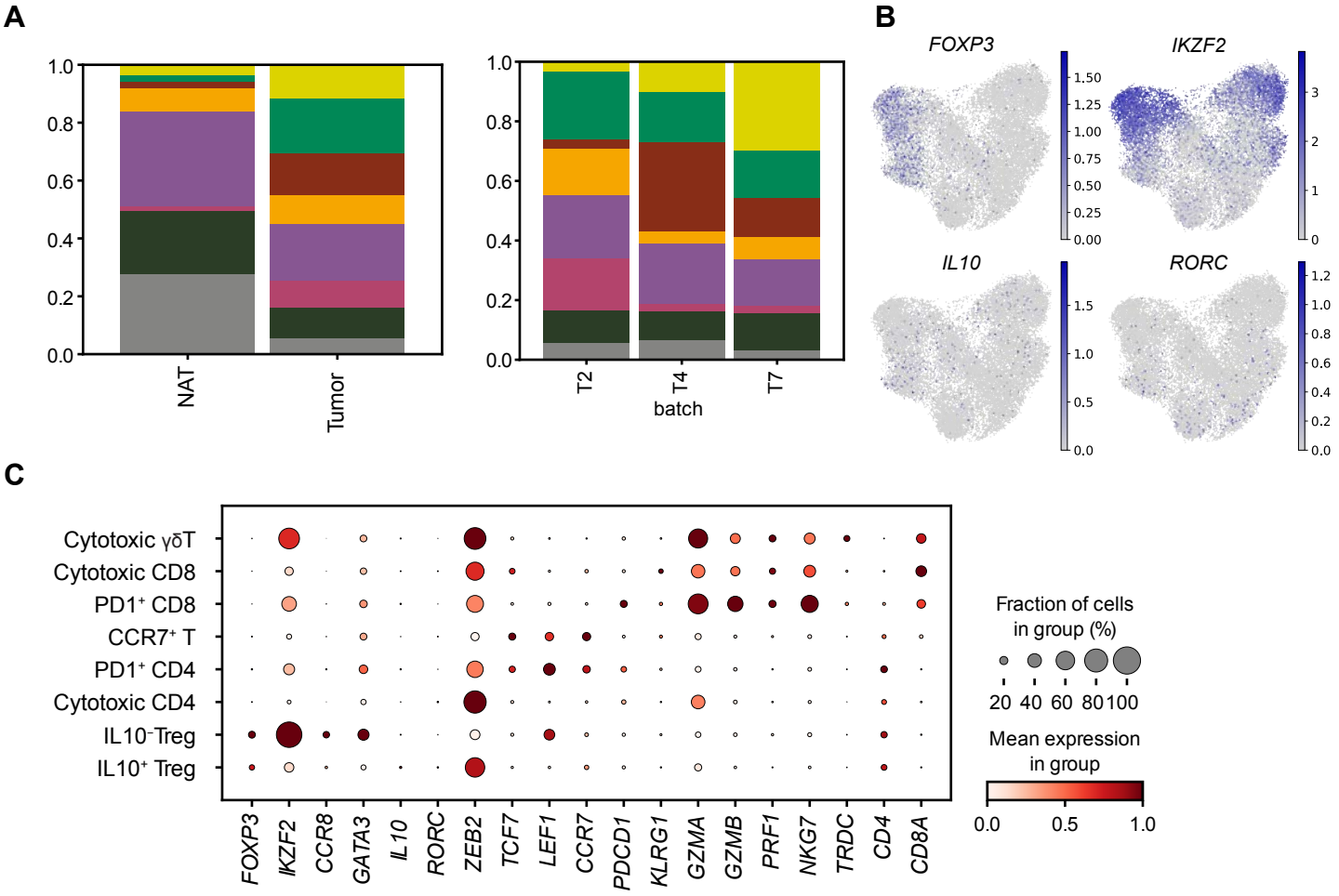
A
1.0
0.8
0.6
0.4
0.2
0.0
NAT
Tumor
T2
T4
T7
batch
B
FOXP3
IKZF2
IL10
RORC
C
Cytotoxic γδT
Cytotoxic CD8
PD1⁺ CD8
CCR7⁺ T
PD1⁺ CD4
Cytotoxic CD4
IL10⁻Treg
IL10⁺ Treg
FOXP3
IKZF2
CCR8
GATA3
IL10
RORC
ZEB2
TCF7
LEF1
CCR7
PDCD1
KLRG1
GZMA
GZMB
PRF1
NKG7
TRDC
CD4
CD8A
Fraction of cells in group (%)
20 40 60 80 100
Mean expression in group
0.0 0.5 1.0

Figure S7

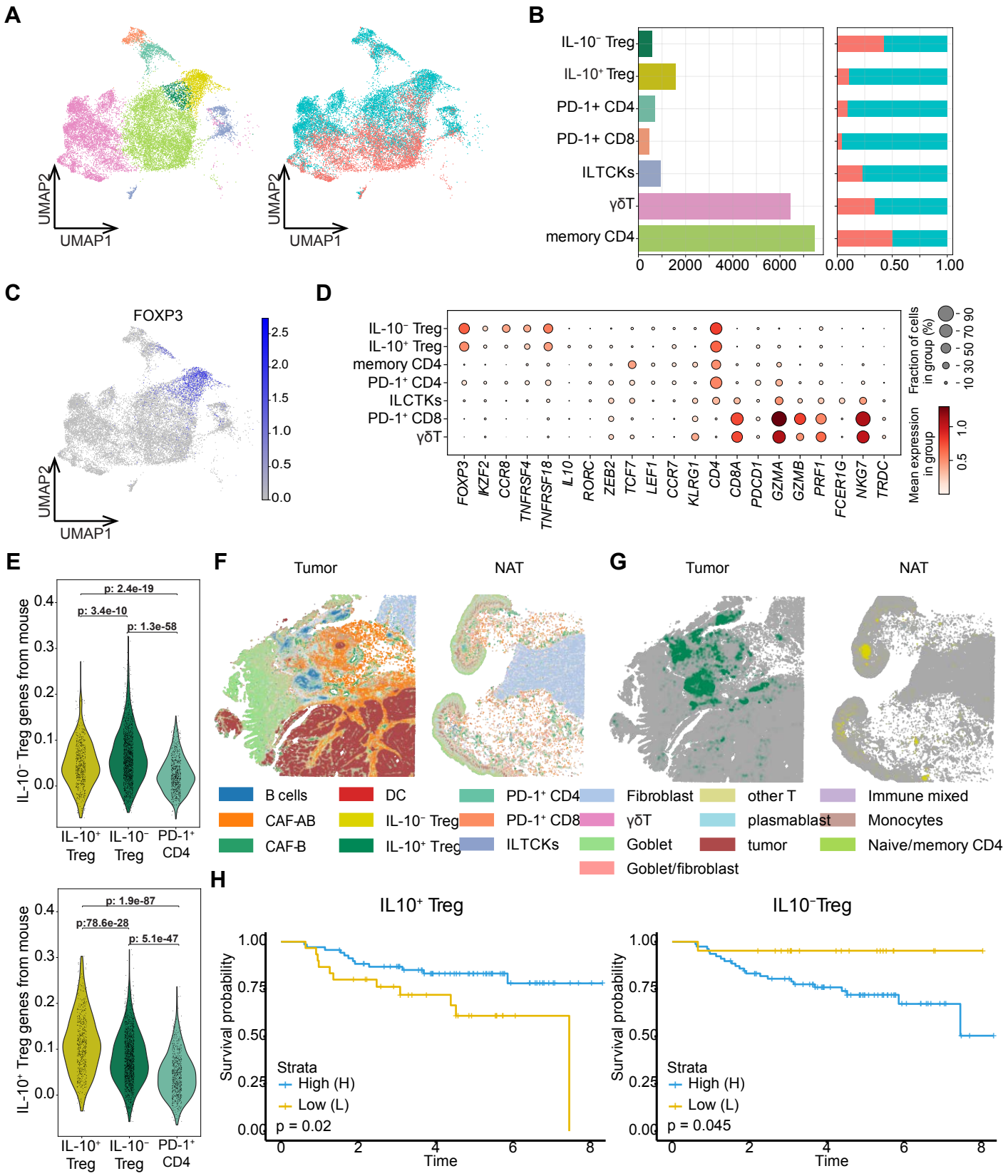
A
UMAP2
UMAP1
B
IL-10⁻ Treg
IL-10⁺ Treg
PD-1+ CD4
PD-1+ CD8
ILTCKs
γδT
memory CD4
0
2000
4000
6000
0.00
0.50
1.00
C
FOXP3
2.5
2.0
1.5
1.0
0.5
0.0
D
Fraction of cells in group (%)
10 30 50 70 90
Mean expression in group
0.5
1.0
FOXP3
IKZF2
CCR8
TNFRSF4
TNFRSF18
IL10
RORC
ZEB2
TCF7
LEF1
CCR7
KLRG1
CD4
CD8A
PDCD1
GZMA
GZMB
PRF1
FCER1G
NKG7
TRDC
E
IL-10⁻ Treg genes from mouse
p: 2.4e-19
p: 3.4e-10
p: 1.3e-58
IL-10⁺ Treg
IL-10⁻ Treg
PD-1⁺ CD4
IL-10⁺ Treg genes from mouse
p: 1.9e-87
p:78.6e-28
p: 5.1e-47
F
Tumor
NAT
G
Tumor
NAT
B cells
CAF-AB
CAF-B
DC
IL-10⁻ Treg
IL-10⁺ Treg
PD-1⁺ CD4
PD-1⁺ CD8
ILTCKs
Fibroblast
γδT
Goblet
Goblet/fibroblast
other T
plasmablast
tumor
Immune mixed
Monocytes
Naive/memory CD4
H
IL10⁺ Treg
IL10⁻Treg
Survival probability
Time
Strata
High (H)
Low (L)
p = 0.02
p = 0.045

Figure S8

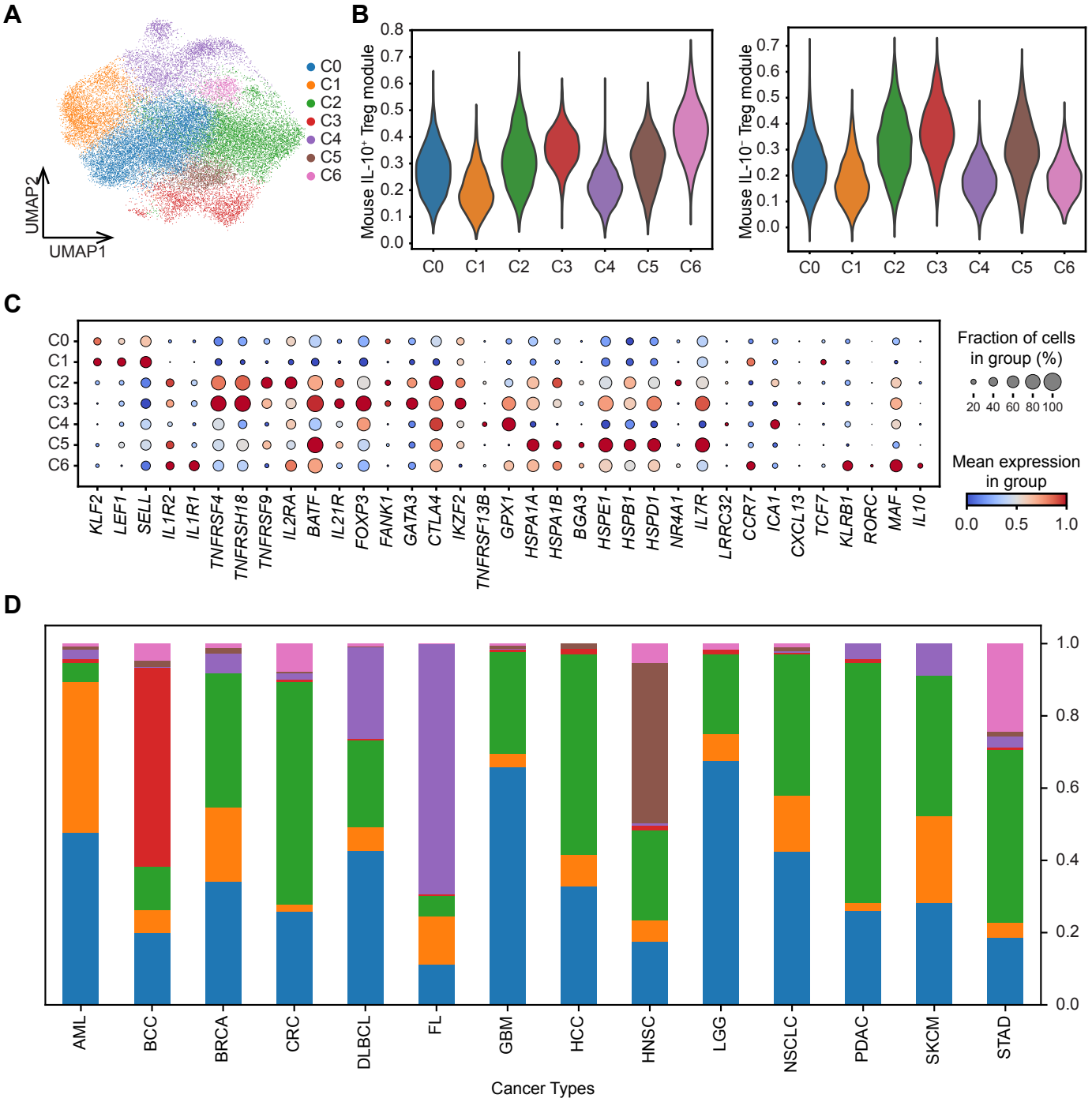
A
C0
C1
C2
C3
C4
C5
C6
UMAP2
UMAP1
B
Mouse IL-10⁺ Treg module
Mouse IL-10⁻ Treg module
C0 C1 C2 C3 C4 C5 C6
C
Fraction of cells in group (%)
20 40 60 80 100
Mean expression in group
0.0 0.5 1.0
KLF2 LEF1 SELL IL1R2 IL1R1 TNFRSF4 TNFRSH18 TNFRSF9 IL2RA BATF IL21R FOXP3 FANK1 GATA3 CTLA4 IKZF2 TNFRSF13B GPX1 HSPA1A HSPA1B BGA3 HSPE1 HSPB1 HSPD1 NR4A1 IL7R LRRC32 CCR7 ICA1 CXCL13 TCF7 KLRB1 RORC MAF IL10
D
AML BCC BRCA CRC DLBCL FL GBM HCC HNSC LGG NSCLC PDAC SKCM STAD
Cancer Types